https://doi.org/10.1093/plphys/kiac494 PLANT PHYSIOLOGY 2023: 191: 177–198

Plant Physiology®

Research Article

Cytosolic phosphoglucose isomerase is essential for microsporogenesis and embryogenesis in Arabidopsis

Hung-Chi Liu [1], Hsiu-Chen Chen,[1] Tzu-Hsiang Huang [1], Wei-Ling Lue [2], Jychian Chen [2] and Der-Fen Suen [1,*]

1 Agricultural Biotechnology Research Center, Academia Sinica, Taipei, Taiwan
2 Institute of Molecular Biology, Academia Sinica, Taipei, Taiwan

*Author for correspondence: suendf@gate.sinica.edu.tw

H-C. L., J. C., and D-F. S. conceived the project, designed and supervised the experiments, and analyzed the data. H-C. L., H-C. C., and W-L. L. performed the experiments. H-C. L. and T-H. H. performed the transcriptome analysis. H-C. L., J. C., and D-F. S. wrote the manuscript. All authors discussed the results and commented on the manuscript.
The author responsible for distribution of materials integral to the findings presented in this article in accordance with the policy described in the Instructions for Authors (https://academic.oup.com/plphys/pages/general-instructions) is: Der-Fen Suen (suendf@gate.sinica.edu.tw).

Abstract

Phosphoglucose isomerase (PGI) catalyzes the interconversion of fructose-6-phosphate and glucose-6-phosphate, which impacts cell carbon metabolic flow. Arabidopsis (*Arabidopsis thaliana*) contains two nuclear *PGI* genes respectively encoding plastidial PGI1 and cytosolic PGI (cPGI). The loss of PGI1 impairs the conversion of F6P of the Calvin–Benson cycle to G6P for the synthesis of transitory starch in leaf chloroplasts. Since *cpgi* knockout mutants have not yet been obtained, they are thought to be lethal. The *cpgi* lethality can be rescued by expressing CaMV 35S promoter (*p35S*)-driven *cPGI*; however, the complemented line is completely sterile due to pollen degeneration. Here, we generated a *cpgi* mutant expressing *p35S::cPGI-YFP* in which YFP fluorescence in developing anthers was undetectable specifically in the tapetum and in pollen, which could be associated with male sterility. We also generated *RNAi-cPGI* knockdown lines with strong cPGI repression in floral buds that exhibited reduced male fertility due to the degeneration of most pollen. Histological analyses indicated that the synthesis of intersporal callose walls was impaired, causing microsporocytes to fail to separate haploid daughter nuclei to form tetrads, which might be responsible for subsequent pollen degeneration. We successfully isolated *cpgi* knockout mutants in the progeny of a heterozygous *cpgi* mutant floral-dipped with sugar solutions. The rescued *cpgi* mutants exhibited diminished young vegetative growth, reduced female fertility, and impaired intersporal callose wall formation in a meiocyte, and, thus, male sterility. Collectively, our data suggest that cPGI plays a vital role in carbohydrate partitioning, which is indispensable for microsporogenesis and early embryogenesis.

Introduction

Primary carbohydrate metabolism provides energy and carbon backbones and is, therefore, essential for the life of cells (Hua et al., 2003). Phosphoglucose isomerase (PGI, EC 5.3.1.9), also known as glucose-6-phosphate isomerase, is a dimeric enzyme that catalyzes the reversible conversion of fructose-6-phosphate (F6P) and glucose-6-phosphate (G6P), two key metabolites involved in several critical cellular processes, such as glycolysis, gluconeogenesis, and the pentose phosphate pathway (Schreyer and Böck, 1980; Sun et al., 1999; Lee et al., 2001; Totir et al., 2012). G6P can be converted to G1P, and then UDP-glucose (UDP-Glc), which can be used as the primary precursor for synthesizing cellular components, such as glycogen, callose, starch, and

Received November 19, 2021. Accepted September 29, 2022. Advance access publication October 22, 2022

glycoconjugates. F6P can undergo glycolysis and citric acid cycle to generate energy and can be converted to pyruvate and then acetyl-CoA, which can be used as the primary precursor for synthesizing several metabolites, such as amino acids and lipids. The regulation of PGI activity may influence the carbon metabolic flow in cells. However, besides the interconversion by PGI, F6P and G6P can also be generated from the phosphorylation of glucose and fructose in the cytosol by hexokinase or fructokinase; therefore, from the point of view of metabolism, cPGI seems dispensable in plant cells.

In plant cells, the PGI reaction is compartmentalized in the cytosol and the plastids/chloroplasts. In Arabidopsis (*Arabidopsis thaliana*), there are two nuclear-encoded *PGI* genes. One is *PGI1* (At4g24620), and the other is *cPGI* (At5g42740), respectively, encoding the plastidial and cytosolic PGI isozymes. The two Arabidopsis PGI isozymes share ∼23% identity and 40% similarity in protein sequences (Yu et al., 2000). Recombinant PGI1 and cPGI have a distinct affinity to G6P and F6P: the K_m of PGI1 for G6P (164 ± 43 μM) is higher than that for F6P (73 ± 80 μM); while the K_m's of cPGI for G6P (158 ± 85 μM) and F6P (203 ± 12 μM) are similar (Preiser et al., 2020). Recombinantly purified cPGI has higher specific activity than its plastidial counterpart originating from wheat, rice, and Arabidopsis (Preiser et al., 2020; Gao et al., 2021). Although the conversion of F6P of the Calvin–Benson cycle to G6P by PGI1 is a critical step for transitory starch synthesis in leaf chloroplasts (Jones et al., 1986; Yu et al., 2000; Kunz et al., 2010), in root tips, the G6P can be alternatively imported from the cytosol making PGI1 dispensable in statolith starch formation (Yu et al., 2000; Kunz et al., 2010). This indicates that different tissues have different carbon metabolic flows suggesting the importance of PGI1 varies among tissues. Moreover, the *pgi1-2* seeds accumulate fewer proteins and fatty acids and are lighter than wild-type (WT) seeds, further suggesting that PGI1 activity contributes to the biosynthesis of storage reserves in the embryo (Bahaji et al., 2018). Engineering of wheat cPGI into chloroplasts of an Arabidopsis *pgi1* mutant leads to starch overaccumulation, increased CO_2 assimilation, and relatively more plant biomass than WT (Gao et al., 2021).

In contrast, knowledge about the biological importance of cPGI in plant growth and development is relatively limited, although putative orthologs of cPGI genes have been studied in various plant species, mainly in the context of the evolutionary history of eukaryotic *PGI* genes (Weeden and Gottlieb, 1982; Thomas et al., 1992, 1993; Nowitzki et al., 1998; Kawabe et al., 2000). The elucidation of cPGI function by mutant analysis has been documented to date in two plant species, Clarkia (*Clarkia xantiana*) and Arabidopsis (Jones et al., 1986; Kunz et al., 2014). In Clarkia, the lost function of either of the two *cPGI* genes leads to reduced levels of overall PGI activity, and both the single mutants (*Cxpgi-2* and *Cxpgi-3*) are viable (Jones et al., 1986). However, no homozygous double null mutant was isolated in the F2 progeny by crossing the two single mutants, suggesting the Clarkia cPGI null mutant is lethal (Jones et al., 1986). Similarly, Arabidopsis T-DNA insertional *cpgi* mutants are only viable as heterozygotes (Kunz et al., 2014). Knockdown of *cPGI* by using the artificial microRNA approach (*amiR-cpgi*) affects carbohydrate metabolism in leaves, which leads to a starch excess phenotype and reduced sucrose contents at the end of the night but not in the daytime (Kunz et al., 2014). Transgenic plants can be obtained with the homozygous *cpgi* mutant background and ectopically expressing the *cPGI* driven by either the constitutive ubiquitin10 promoter (*pUBQ10*), the Cauliflower mosaic virus 35S promoter (*p35S*), or the seed-specific unknown seed protein promoter (*pUSP*). Interestingly, among these complemented lines, the plants harboring *pUBQ10*-driven cPGI are fertile, whereas those harboring *pUSP* or *p35S* grow normally but are completely male sterile (Kunz et al., 2014). These results suggest that cPGI is required for normal male fertility. However, why and for which processes cPGI is essential are still unclear.

To study the role of cPGI in pollen development, we generated a transgenic line of the T-DNA knockout mutant *cpgi-3*$^{(-/-)}$ expressing a *p35S*-driven transgene encoding cPGI fused with yellow fluorescent protein (*p35S::cPGI-YFP*). In addition, *p35S::RNAi-cPGI* knockdown lines (*Ri-cpgi*) with strong cPGI repression in developing floral buds exhibited greatly reduced male fertility due to defective pollen development. Histological analyses demonstrated the synthesis of intersporal callose walls was impaired in a meiocyte so that it failed to separate the four daughter nuclei to form a tetrad microspore, which might lead to subsequent pollen degeneration. In addition, the embryo carrying homozygous *cpgi-3* alleles developing in siliques of heterozygous mutants seemed impaired at pre-globular stage. Amazingly, we were able to obtain *cpgi* knockout mutants using a strategy of floral sugar feeding to alleviate the cPGI indispensability in young embryogenesis for producing viable *cpgi* mutant seeds. The rescued *cpgi* knockout mutants exhibited diminished young vegetative growth, reduced female fertility, and defective intersporal callose wall formation that led to male sterility. Our results suggest that cPGI plays an indispensable role during microsporogenesis and early embryogenesis in Arabidopsis. Possible roles of cPGI in carbohydrate partitioning in these critical reproductive processes are discussed.

Results

Generation of *cpgi* knockout mutant expressing *p35S::cPGI-YFP* for phenotypic analysis of its male sterility

Kunz et al. (2014) have reported a puzzle that *p35S*-driven *cPGI* cannot complement the defect of male sterility in the *cpgi*$^{(-/-)}$ mutant background. A possibility is the 35S promoter is not active during pollen development. To gain further insight into the mechanism, we isolated the *p35S::cPGI-YFP cpgi*$^{(-/-)}$ plants (Figure 1; Supplemental Table S1) from the F2 progeny of crossing the *p35S::cPGI-YFP* transformants (in WT background) with the *cpgi* T-DNA mutant

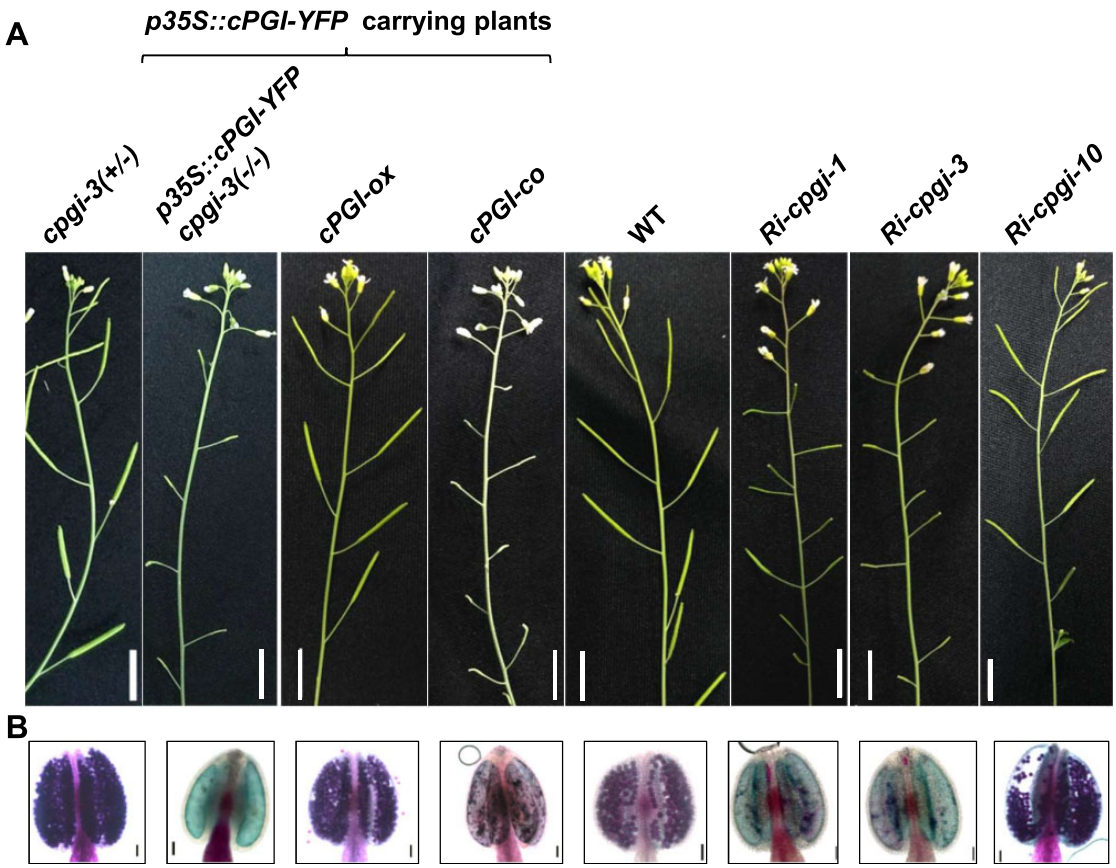

Figure 1 Reduced male fertility found in different cPGI-deficient lines. A, A representative inflorescence stem showing the seed setting of the heterozygous *cpgi-3*$^{(+/-)}$ mutant, the *cpgi* knockout mutant expressing *p35S::cPGI-YFP* [*p35S::cPGI-YFP cpgi-3*$^{(-/-)}$], the transgenic line overexpressing *p35S::cPGI-YFP* (*cPGI-ox*), the *cPGI* co-suppressed line (*cPGI-co*), the WT plant (Col-5), and the RNAi knockdown lines *Ri-cpgi-1*, *Ri-cpgi-3*, and *Ri-cpgi-10*. B, Alexander-stained whole-mount anthers were inspected using light microscopy for the viability of mature pollen. A representative image is shown for the plants shown in the same column in (A). Note that most of the pollen degenerated in those plants, producing mostly seedless siliques, while *cpgi-3*$^{(+/-)}$, *cPGI-ox*, WT, and *Ricpgi-10* plants produced viable pollen and thus produced fertile siliques. Bars in (A) and (B) are 1 cm and 50 μm, respectively.

line GK-013D09 (designated as *cpgi-3*). The *cpgi-3* mutant harbors sulfadiazine (Sul) resistance allowing a convenient screening for progenies carrying the *cpgi-3* allele. The heterozygous *cpgi-3*$^{(+/-)}$ plants were used for the crosses with the *p35S::cPGI-YFP* transformants because no *cpgi-3*$^{(-/-)}$ plants were obtained among a total of 729 descendants screened in the self-pollinated progeny of *cpgi-3*$^{(+/-)}$ under typical soil-grown conditions (Supplemental Table S2), which was consistent with previously reported homozygous lethality in *cpgi-1* and *cpgi-2* T-DNA mutants (Kunz et al., 2014). Intriguingly, $<5\%$ of the F2 progeny were *p35S::cPGI-YFP cpgi-3*$^{(-/-)}$ plants (Supplemental Table S1), which diverged considerably from the Mendelian segregation. Similarly, only three of the *p35S::cPGI-YFP cpgi-3*$^{(-/-)}$ plants were isolated among a total of 107 screened descendants (~2.8%) of cross-pollinating an F1 dihybrid (*p35S::cPGI-YFP/- cpgi-3*$^{+/-}$) with pollen grains from a *cpgi-3*$^{(+/-)}$ plant (Supplemental Table S1 and Supplemental Figure S1A), which was also much less than the expected segregation.

All the *p35S::cPGI-YFP cpgi-3*$^{(-/-)}$ plants isolated were completely male sterile due to pollen degeneration (Figure 1; Supplemental S1B), consistent with the previously reported *p35S::cPGI cpgi-1*$^{(-/-)}$ sterility (Kunz et al., 2014). The expression of the cPGI-YFP fusion protein (deduced molecular mass 90 kDa) and no expression of the endogenous cPGI protein (deduced molecular mass 61.7 kDa) in the *p35S::cPGI-YFP cpgi-3*$^{(-/-)}$ plants was further verified by immunoblot analyses using the antibody against the cPGI we generated (Supplemental Figure S1D). Enzyme activity of the cPGI-YFP fusion protein and undetectable endogenous cPGI activity was further confirmed using an in-gel PGI activity assay (Supplemental Figure S1E).

In the cPGI overexpressed lines (*p35S::cPGI-YFP* transgenic plants in either WT or *cpgi-3* + /− background; *cPGI-ox*), there were two functional cPGIs, the endogenous one and the cPGI-YFP fusion protein (Supplemental Figure S1D), both having enzyme activity as verified by in-gel PGI activity assay (Supplemental Figure S1E). In addition to its homodimer, the two seemed to be able to form a heterodimer since a major band of cPGI-YFP (possibly a homodimer) was found in both the *cPGI-ox* plants and the *p35S::cPGI-YFP cpgi-3*$^{(-/-)}$ plants, while an additional minor band (possibly a

heterodimer of cPGI-YFP and endogenous cPGI) below the major band was found only in the *cPGI-ox* plants (Supplemental Figure S1E). Heterodimerization between the two monomers of Clarkia cytosolic CxPGI-2 and CxPGI-3 revealed by zymogram (Jones et al., 1986) supports our interpretation.

Although only limited numbers of *p35S::cPGI-YFP cpgi-3*$^{(-/-)}$ plants have been obtained, these plants were used for visualizing YFP signals in developing anthers and for phenotypic analyses regarding their defective pollen development.

YFP signals were undetectable restrictedly in the tapetum and pollen in developing anthers of *p35S::cPGI-YFP cpgi-3*$^{(-/-)}$ plants

YFP fluorescence was detected in the *p35S::cPGI-YFP* expressing transformants (Figure 2; Supplemental Figures S1C and S2). In developing anthers, the YFP signals were detectable in the epidermis, endothecium, and connecting tissues of the anther, where the cells contained differentiated chloroplasts showing chlorophyll autofluorescence under confocal microscopy (Figure 2). Dual localization of cPGI-YFP in the cytoplasm and the nucleus were observed in the epidermal and endothecial cells of anthers (Figure 2, A′ and B′), as well as in leaf epidermis (Supplemental Figure S1C, using the T1-2 transformant as an example). In contrast, the YFP signals were very low or undetectable in developing pollen and the tapetum (the innermost layer of anther wall that nurtures pollen development), where those cells contain nonphotosynthetic plastids, thus lacking chlorophyll autofluorescence (Figure 2, C and C′; Supplemental Figure S1C). The YFP signals in the tapetum and pollen were undetectable across all examined developmental stages of anthers (Supplemental Figure S2). Thus, the male sterility in *p35S::cPGI-YFP cpgi-3*$^{(-/-)}$ plants might be associated with undetectable *cPGI* expression in the tapetum and pollen.

Arabidopsis *cPGI* is expressed in most tissues and is at a relatively high level during pollen and embryo development compared to other tissues

To understand *cPGI* expression in Arabidopsis, especially in reproductive tissues, an in silico analysis was performed by using publicly accessible transcriptome datasets (Honys and Twell, 2004; Klepikova et al., 2016; Li et al., 2017; Waese et al., 2017; Hofmann et al., 2019) compiled by the Arabidopsis eFP Browser (Winter et al., 2007). The relative abundance of *cPGI* transcripts to the reference gene *ACTIN 8* (*ACT8*; At1g49240) in the selected tissues was profiled (Supplemental Figure S3, A–D). The result displayed that the *cPGI* transcripts were detected in all tissues examined across various developmental phases, indicating the ubiquitous expression nature of *cPGI* in Arabidopsis. The expression of *cPGI* was also verified in a tapetum-specific transcriptome (Li et al., 2017). The expression levels of *cPGI* were relatively high in seedling cotyledons, young leaves, flowers, anthers of young flower, ovules, young seeds (Supplemental Figure S3A), and the tapetum (Supplemental Figure S3B) compared to those in roots and opened anthers (Supplemental Figure S3A). The levels of cPGI expression were relatively high during microgametogenesis (young microspore to tricellular pollen stage; Supplemental Figure S3C) and embryo development (Supplemental Figure S3D). We further confirmed the abundance of *cPGI* transcripts by reverse transcription–quantitative polymerase chain reaction (RT–qPCR) analysis, which showed relatively high levels in stamens and pistils than in seedlings (Supplemental Figure S3E). The abundance of cPGI protein was also relatively high in floral buds and young siliques than in shoots and roots of 14-day-old seedlings (Supplemental Figure S3F). These results indicated that *cPGI* is expressed in the tapetum and pollen during pollen development.

Strong repression of cPGI in developing floral buds corresponded to the reduction of male fertility in Arabidopsis

In addition to the phenotypically normal *cPGI-ox* plants that produced fertile siliques and viable pollen as the WT (Figure 1; Supplemental Figure S1B), we also found that among 14 T1 transformants carrying *p35S::cPGI-YFP* under WT background, six of them produced mostly seedless siliques (*cPGI-co* line in Figure 1A and the A1 plant in Supplemental Figure S1B). The markedly reduced fertility was also associated with pollen degeneration, which was similar to the phenotypes of *p35S::cPGI-YFP cpgi-3*$^{(-/-)}$ plants (Figure 1B and the A5 plant in Supplemental Figure S1B). In addition, YFP signals were hardly detectable in these transformants (Supplemental Figure S1C), pointing toward the phenomenon of transgene-induced post-transcriptional gene silencing, which is termed co-suppression in plants (Napoli et al., 1990; van der Krol et al., 1990; Cogoni and Macino, 1997; Vaucheret et al., 1998). Not only the cPGI-YFP fusion protein but also the endogenous cPGI were greatly suppressed to nearly undetectable levels in these *cPGI* co-suppressed plants (*cPGI-co*; Figure 3D; Supplemental S1, D and E). The *cPGI-co* plants also appeared in some of the T2 descendants of *cPGI-ox* lines and some progenies of the cross between *p35S::cPGI-YFP cpgi-3*$^{(+/-)}$ and *cpgi-3*$^{(+/-)}$ plants (such as the A1, A3, and A6 siblings shown in Supplemental Figure S1 as an example). The *cPGI-co* plants provided a line of evidence that strong *cPGI* repression would lead to defective pollen development; however, they produced on average only ∼2% elongated siliques with very few viable seeds (Figure 3B). Besides this, the reversion of co-suppression phenotypes may occur in progenies (Cogoni and Macino, 1997). The unstable gene silencing status of *cPGI-co* lines made them not a suitable source to stably provide plant materials for investigating the mechanism of cPGI-deficiency-induced male sterility.

To circumvent this difficulty, we further generated *cPGI* downregulated mutants by expressing *p35S*-driven double-stranded RNA interference (RNAi). Several independent *RNAi-cPGI* (*Ri-cpgi*) lines were isolated, and three independent lines, *Ri-cpgi-1*, *Ri-cpgi-3*, and *Ri-cpgi-10*, were selected

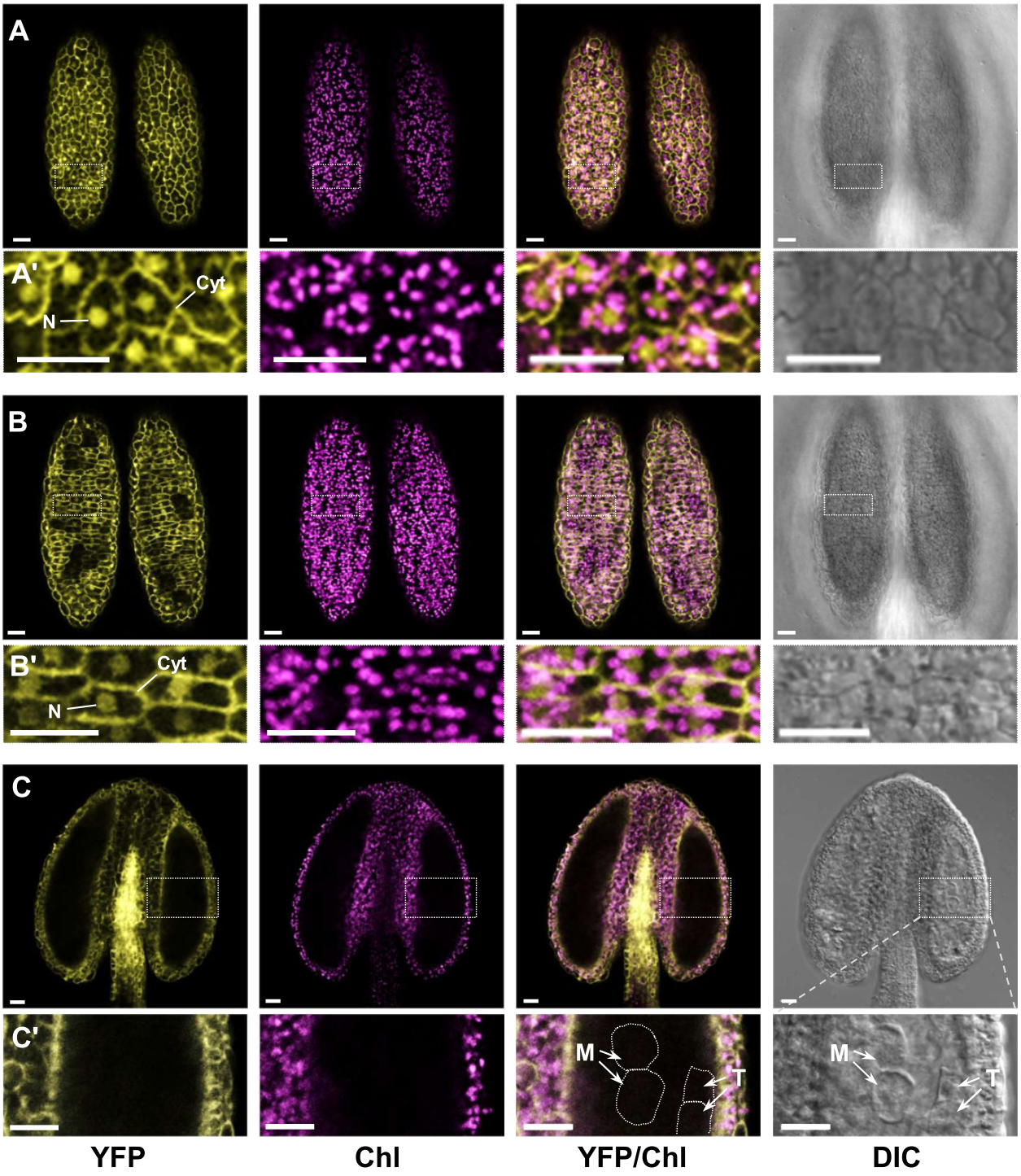

Figure 2 Subcellular localization and distribution of cPGI-YFP fusion proteins in developing anthers of the partially complemented *p35S::cPGI-YFP cpgi-3*$^{(-/-)}$ plants. A,B, Optical sections of confocal microscopy focusing on the layer of the epidermis (A) and of endothecium (B) of the same anther dissected from a 1.2-mm floral bud (corresponding to the late binucleate pollen stage in WT plants) of a sterile *p35S::cPGI-YFP cpgi-3*$^{(-/-)}$ plant. Dual localization in the nucleus (N) and cytoplasm (Cyt) was observed in those cells expressing *p35S::cPGI-YFP* (A′ and B′). C, A longitudinally optical section focusing on the locular space of an anther dissected from another 0.5-mm bud (corresponding to the meiosis pollen stage in WT plants). Note the YFP signals were detected in the epidermis, endothecium, and connecting tissues of the anther, where those cells contained differentiated chloroplasts; while the signals were undetectable in the tapetal cells (T) and the callose wall-encased meiocytes (M), in which do not contain differentiated chloroplasts (C′). Parts from left to right respectively show the channel of yellow fluorescent protein (YFP), chlorophyll autofluorescence (Chl), the merged (YFP/Chl), and DIC. Bars = 20 μm.

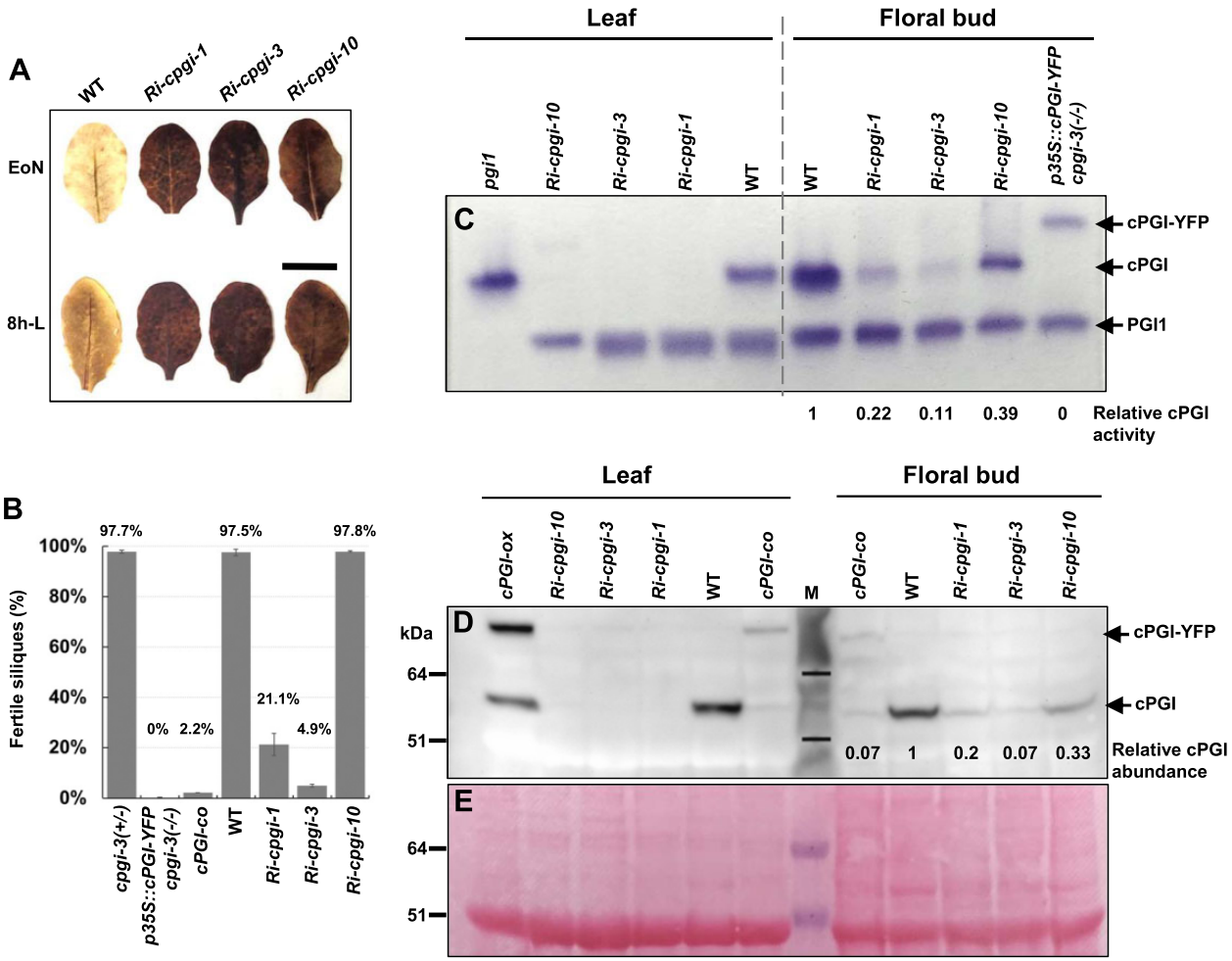

Figure 3 Evaluation of cPGI repression and fertility in *Ri-cpgi*, *cPGI-co*, and *p35S::cPGI-YFP cpgi-3*$^{(-/-)}$ lines. A, Starch-excess phenotypes in *Ri-cpgi* lines. Mature, unshaded leaves were harvested at the end of night (EoN) or 8 h into light (8h-L) from 5-week-old plants grown under a 16-h light/8-h dark regime for iodine staining for starch content. Bar = 1 cm. B, The fertility of the indicated plants was evaluated by calculating the percentage of elongated siliques (seed-containing) over the total siliques scored. The percentage mean ± SE is plotted, and the percentage mean of each line is indicated (plant n = 3–8). C, Soluble proteins extracted from rosette leaves and inflorescence apices (floral buds in various sizes) of the same plants as indicated were subjected to nondenaturing polyacrylamide gel electrophoresis for the in-gel PGI activity assay. The PGI enzyme activity was shown as a purple band of formazan precipitation on the gel. The activity of plastidial PGI1, endogenous cPGI, and the cPGI-YFP fusion protein was as indicated. D, Immunoblotting assay using the primary antibodies against cPGI. E, After immunoblotting, to show the abundance of loaded proteins, the blot was stained with Ponceau S, showing the major protein band of Rubisco large subunit as a reference; the same blot region is shown as in (D). The molecular mass of protein markers (M) is indicated in kDa at the left. Relative cPGI enzyme activity (C) or cPGI protein abundance (D) to that of WT levels in floral buds was evaluated by ImageJ quantification.

for further analyses based on their varying degrees of reduced male fertility (Figures 1, A and 3, B). On an average, ~21% and 5% of elongated siliques were produced in *Ri-cpgi-1* and *Ri-cpgi-3* plants, respectively (Figure 3D); many of the elongated siliques contained <50% WT seed number (Supplemental Figure S4, D–F). Female fertility of *Ri-cpgi-1* and *Ri-cpgi-3* was not impaired as judged by setting seeds normally as WT after pollinating with WT pollen grains (Supplemental Figure S4, G and H). Thus, the reduced fertility in *Ri-cpgi-1* and *Ri-cpgi-3* was attributed to defective pollen development, which was similar to that in the *cPGI-co* plants (Figure 1B). In contrast, the *Ri-cpgi-10* line produced viable pollen and was fertile as the WT (Figures 1 and 3, B). The phenotypes of these *Ri-cpgi* lines were stably inherited in their progenies.

These *Ri-cpgi* lines exhibited slightly but significantly diminished vegetative growth (especially *Ri-cpgi-10*; Supplemental Figure S4, A and B) compared to the WT, but their flowering times were not apparently affected under our growth conditions (Supplemental Figure S4C). All the three *Ri-cpgi* lines accumulated excessive starch in leaves (Figure 3A), and such phenotypes were consistent with the previously reported mutants with *cPGI* downregulation by the artificial microRNA approach (*amiR-cpgi*; Kunz et al., 2014). The starch-excess phenotypes were highly associated with strong cPGI repression in rosette leaves of all the three

Ri-cpgi lines examined, as revealed by in-gel PGI activity assay and immunoblot analysis showing nearly undetectable levels of endogenous cPGI in leaves (Figure 3, C–E).

In contrast, the effects of *RNAi*-mediated gene silencing varied in developing floral buds among these *Ri-cpgi* lines (Figure 3, C and D). Residual cPGI activity seemed proportional to the cPGI protein abundance (Figure 3, C and D, right half of the gel/blot). In addition, the protein abundance of endogenous cPGI in *cPGI-co* buds was comparable to that in *Ri-cpgi-3* buds (∼7% WT level of endogenous cPGI, Figure 3D). Interestingly, the levels of cPGI repression seemed highly related to the severity of reduced fertility: a stronger cPGI repression in *cPGI-co* and *Ri-cpgi-3* associated with producing 2% and 5% fertile siliques, while a milder cPGI repression in *Ri-cpgi-1* (∼20% WT level) associated with producing 21% fertile siliques (Figure 3B). Although the cPGI abundance was repressed to ∼33% WT cPGI abundance, the *Ri-cpgi-10* plants produced 97.8% fertile siliques, which was comparable to the WT (Figure 3B). These results suggested that repression of cPGI function in developing floral buds to below a threshold would impair pollen development and thus resulting in a reduction of male fertility.

Loss of cPGI impaired microsporogenesis in Arabidopsis

To understand at which stages of pollen development were affected, we inspected anthers in developing floral buds clustered in an inflorescence apex by using semi-thin cross-sectioning (Figure 4). We previously reported a linkage between pollen developmental stage and longitudinal sizes of WT floral buds (Chen et al., 2019). It was applied for phenotypical comparison of the progression of pollen development in *Ri-cpgi-3* and *p35S::cPGI-YFP cpgi-3*$^{(-/-)}$ plants. Since the development of floral organs was not apparently impaired in *Ri-cpgi* lines and *p35S::cPGI-YFP cpgi-3*$^{(-/-)}$ plants (Supplemental Figures S5 and S6), the bud size was used here as a reference for the developmental stages of anthers and pollen for the phenotypical comparison between WT and mutant lines. Floral buds ranging from 0.5-mm to 1.0-mm sizes were analyzed (Figure 4). In WT, callose wall-encased meiocytes undergoing meiosis were usually found in anthers of 0.5-mm buds. Tetrad microspores, usually found in 0.6-mm buds, formed after the meiocytes finish the second meiotic division and the synthesis of the intersporal callose wall to complete cytokinesis. Afterward, the callose walls of tetrads were dissolved by the callase enzyme secreted from the tapetal cells to release the haploid young microspores (YM) that were often observed in 0.7-mm buds. Vacuolated and binucleate pollen (resulting from pollen mitosis I) were usually found in 0.8-mm and 1.0-mm buds, respectively (Figure 4; Owen and Makaroff, 1995; Chen et al., 2019). In *Ri-cpgi-3*, the developing pollen in anthers of 0.5- to 0.7-mm buds resembled the meiocytes in 0.5-mm WT buds. Multinucleate pollen was observed in 0.7- to 0.8-mm buds. Degenerated pollen debris was observed in 1.0-mm buds. Intriguingly, tetrad microspores were not observable across the progression analyzed in the *Ri-cpgi-3* buds (Figure 4; middle). Similar pollen defects were observed in *p35S::cPGI-YFP cpgi-3*$^{(-/-)}$, such as multinucleate pollen (in 0.6-mm buds), degenerated pollen debris (in 0.7- to 1.0-mm buds), and no observable tetrad microspores (Figure 4, bottom). Additionally, the enlarged and vacuolated tapetal cell was another common difference found in the anthers of 0.6-mm to 1.0-mm buds in *Ri-cpgi-3* and *p35S::cPGI-YFP cpgi-3*$^{(-/-)}$ plants compared to those showing a thin and compact tapetal layer in the WT (Figure 4). The observed anther defects illustrated the manifestation of male sterility in the mutants lacking sufficient cPGI. The results also suggested that the critical stage of pollen development in response to cPGI deficiency was the transition from meiosis to the tetrad stage.

Since callose wall formation is an essential step in forming the tetrad microspores, aniline blue staining, a fluorescent dye to stain callose walls (Dong et al., 2005; Lu et al., 2014), was performed to confirm whether the formation of callose walls was impaired. In the WT, the callose signals were not detectable in the anthers of 0.4-mm buds (corresponding to pollen mother cell (PMC) stage; Supplemental Figure S6). Strong signals were detected in anthers of 0.5-mm and 0.6-mm buds, reflecting the callose wall-encased meiocytes and the tetrads, respectively (Figure 5; Supplemental Figure S6). The callose signals became undetectable in anthers of 0.7-mm buds (and afterward) since the callose walls of tetrad microspores were dissolved to release YM in the WT (Supplemental Figure S6). However, the callose signals were detectable in the anthers of 0.5-mm to 0.7-mm buds in the *Ri-cpgi-1*, *Ri-cpgi-3*, and *p35S::cPGI-YFP cpgi-3*$^{(-/-)}$ plants (Supplemental Figure S6). The callose signals were nearly undetectable in 0.8-mm buds, suggesting callose dissolution occurred within 0.7- to 0.8-mm buds of those plants (Supplemental Figure S6). When examining the morphology of developing pollen released from the aniline blue-stained anthers in *Ri-cpgi-1*, the meiocytes enclosed by the outer callose wall were observed in 0.5- to 0.6-mm buds. Tetrad-like microspores containing thin intersporal callose walls were found in some 0.7-mm buds of *Ri-cpgi-1* lines (Figure 5, middle). The pollen from 0.7-mm buds of *Ri-cpgi-3* lines with severe *cPGI* knockdown in inflorescences and those from 0.6-mm buds of *p35S::cPGI-YFP cpgi-3*$^{(-/-)}$ plants were all encased only by the outer callose wall but without visible intersporal callose walls (Figure 5, bottom). Moreover, it seemed like the outer callose walls were dissolved before the formation of intersporal callose walls in *Ri-cpgi-3* (0.8-mm buds) and in *p35S::cPGI-YFP cpgi-3*$^{(-/-)}$ plants (0.7-mm buds; Figure 5, bottom). These results suggested that the formation of intersporal callose walls was likely impaired.

Synthesis of callose walls of meiocytes requires the activity of callose synthases (CalS; also called GLUCAN SYNTHESE-LIKE, GSL). In Arabidopsis, synthesis of the outer callose wall that encases a meiocyte requires CalS5 (Dong et al., 2005; Nishikawa et al., 2005). To finish male meiosis, the process of formation of intersporal callose wall to separate daughter

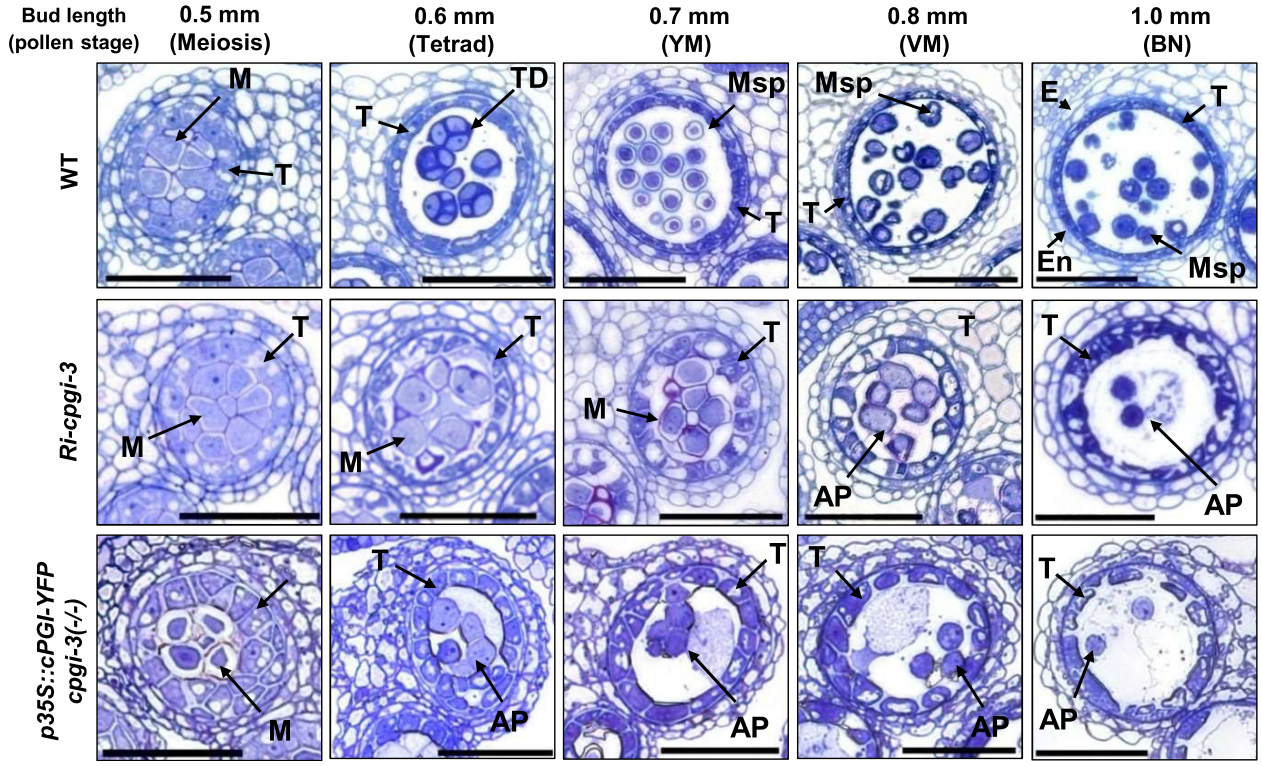

Figure 4 Anther defects in *Ri-cpgi-3* and *p35S::cPGI-YFP cpgi-3*$^{(-/-)}$ plants. Representative micrographs show one of the four locules in semi-thin cross-sections of anthers from the indicated length of developing floral buds in the WT (top), *Ri-cpgi-3* (middle), and *p35S::cPGI-YFP cpgi-3*$^{(-/-)}$ (bottom) plants. The pollen stages corresponding to the bud sizes in WT plants are indicated in parentheses. AP, abnormal pollen; E, epidermis; En, endothecium; M, meiocyte; Msp, microspore; T, tapetum; TD, tetrad; YM, young microspore stage; VM, vacuolated microspore stage; BN, binucleate pollen stage. Bars = 50 μm.

nuclei relies on either *CalS11* (*GSL1*) or *CalS12* (*GSL5*), the two functionally redundant genes. The *cals11*$^{(+/-)}$ *cals12*$^{(-/-)}$ mutant is male sterile due to the defects in synthesizing intersporal callose walls in meiocytes, but the single mutant *cals11* or *cals12* is phenotypically normal (Enns et al., 2005). Additionally, the Arabidopsis T-DNA mutant defected in *CALLOSE DEFECTIVE MICROSPORE1* (*CDM1*) gene exhibit altered expression of *CalS5*, *CalS12*, and of callase-related genes (such as a callase gene *At3g24330*), resulting in defective callose deposition and thus eventually male sterility (Lu et al., 2014). Therefore, we performed RT–qPCR to check the expression of *CalS5*, *CalS11*, *CalS12*, and *At3g24330* in the *Ri-cpgi* lines (Supplemental Figure S7). In the anthers collected from 0.5- to 0.8-mm buds, the relative transcript levels of *CalS5* in *Ri-cpgi* lines were higher than that of WT; those of *CalS11* were lower in *Ri-cpgi-3* and *Ri-cpgi-10* lines; while those of *CalS12* were comparable between WT and *Ri-cpgi* lines (Supplemental Figure S7). The results suggested that the defects of intersporal callose walls found in *Ri-cpgi-1* and *Ri-cpgi-3* were not due to inhibition of the responsible genes *CalS11* and *CalS12*.

To understand whether meiotic divisions of male meiosis were affected, we further assessed the chromosomal morphology (Ma, 2006) in *Ri-cpgi-3* and WT meiocytes using 4′,6-diamidino-2-phenylindole (DAPI) staining (Figure 6, A–J). In 0.5-mm buds of WT plants, the typical meiotic progression could be observed in the outer callose wall-encased meiocytes (Figure 6, A–C). The tetrad pollen stage is usually found in 0.6-mm buds of the WT, as shown by divided haploid nuclei compartmented by thick intersporal callose walls (Figure 6D). Followed by dissolution of the callose walls, in 0.7-mm buds, the haploid YM are released from tetrads (Figure 6E). However, in the *Ri-cpgi-3* line, the progression of meiotic division from metaphase I to telophase II characterized by the DAPI-stained chromosome morphology was observable in 0.5- to 0.7-mm buds (Figure 6, F–H). In 0.8-mm buds (and afterward), the callose wall-dissolved pollen in which the chromosomes looked condensed seemed still undergoing meiotic progression (Figure 6, I and J), reflecting an incomplete meiotic process when callose dissolution occurred. This was further supported by the observation of multinucleated pollen in the anthers of another 0.8-mm bud of *Ri-cpgi-3* using transmission electron microscopy (TEM; Figure 6, K and L), which indicated that meiotic nuclear division could be completed, but the process of formation of intersporal callose wall to separate daughter nuclei was impaired. To conclude, the data from aniline blue staining, DAPI staining, and TEM suggested that the male-sterility induced by cPGI-deficiency was likely due to impaired formation of

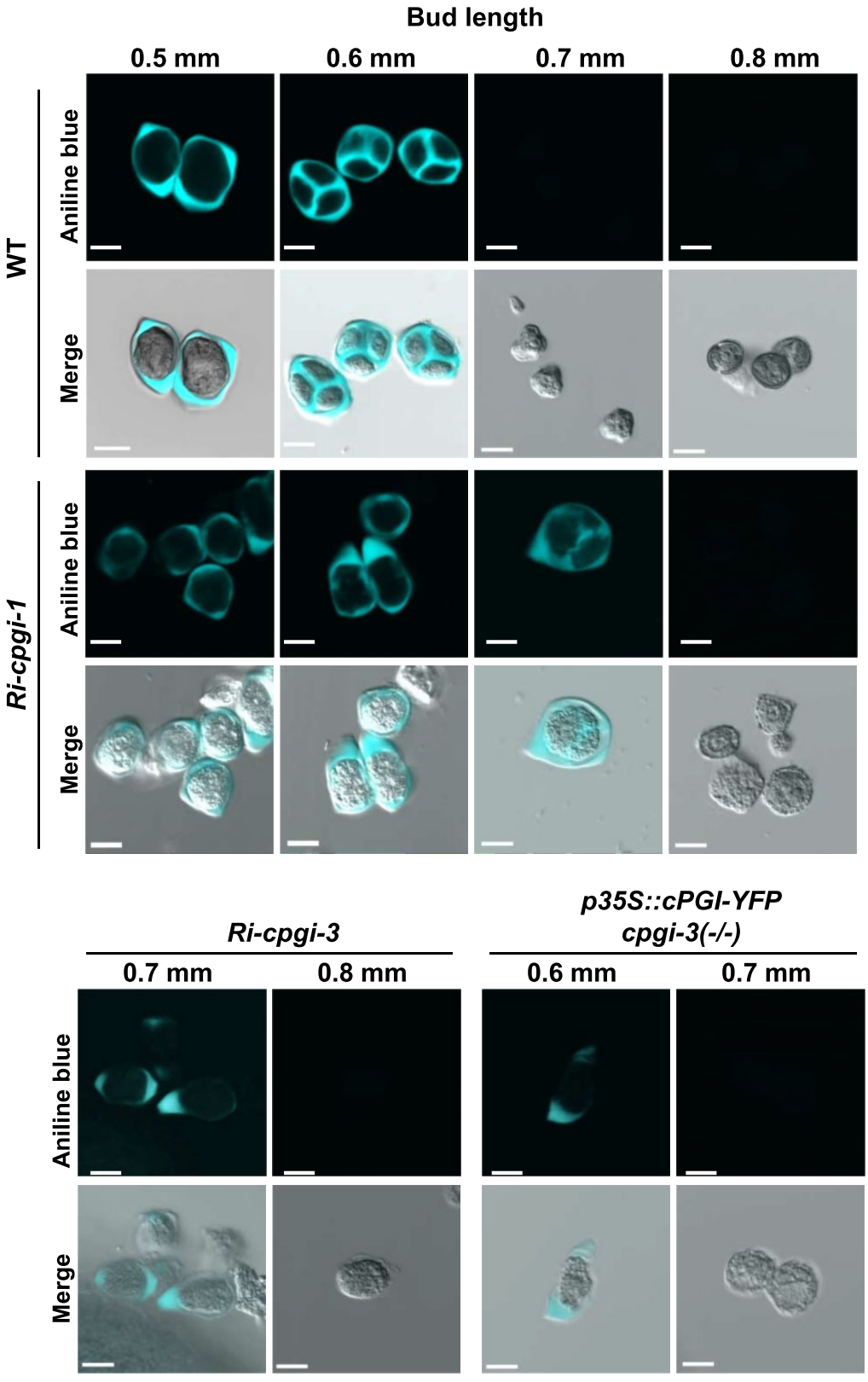

Figure 5 Impaired formation of intersporal callose walls during microsporogenesis in *Ri-cpgi-1*, *Ri-cpgi-3*, and *p35S::cPGI-YFP cpgi-3*$^{(-/-)}$ plants. Developing pollen isolated from the aniline blue-stained anthers (Supplemental Figure S6) of the indicated length of floral buds was inspected using confocal microscopy. The aniline blue-callose fluorescence is artificially colored in cyan (top), and the image merged with the DIC channel is shown in the bottom. Bars = 10 μm.

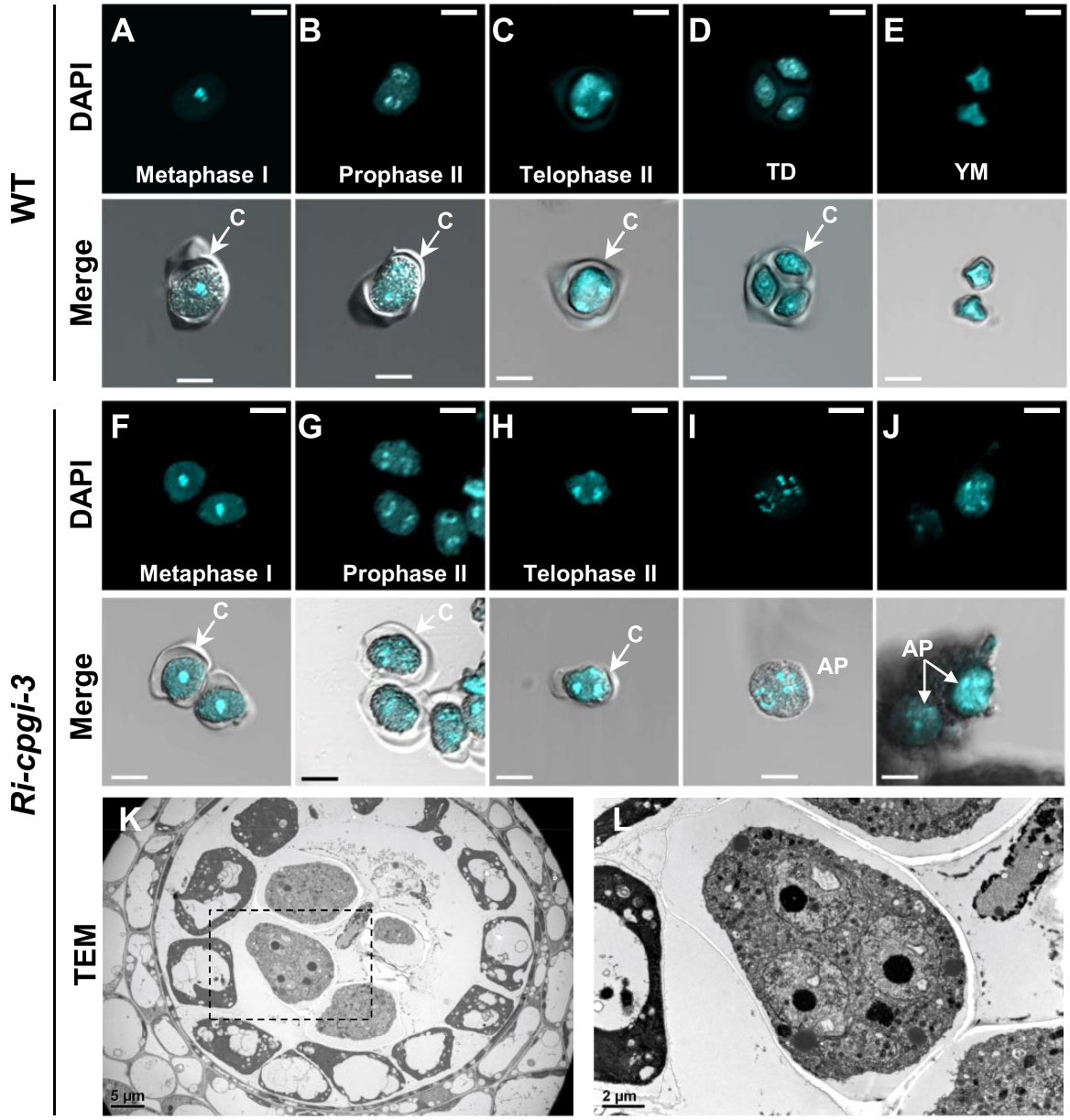

Figure 6 Incomplete cytokinesis of male meiosis in the *Ri-cpgi-3* mutants. A–J, Using DAPI staining to visualize the chromosomal morphology in callose wall encased (indicated as "C" in images) meiocytes, tetrad microspores (TD), or in YM (released from the tetrads after callose dissolution) in WT plants (A–E) and the corresponding processes in the *Ri-cpgi-3* plants (F–J) by confocal microscopy. Shown are representative micrographs of the DAPI channel (top in A–J) and the merged channels of DAPI and differential interference contrast (bottom in A–J). Meiotic stages were determined from the DAPI-stained morphology. Note the pollen shown in (A–C) from different 0.5-mm buds, (D) from 0.6-mm buds, and (E) from 0.7-mm buds of WT plants; while those shown in (F–H) were from 0.6-mm to 0.7-mm buds of *Ri-cpgi-3* plants. Abnormal pollen (AP) found in 0.8-mm buds of *Ri-cpgi-3* plants resembled a meiocyte undergoing anaphase II (I) or telophase II (J) but whose outer callose wall was dissolved before forming a tetrad, indicating incomplete microsporogenesis. (K–L) TEM analysis of a cross-section of an anther from another 0.8-mm bud of *Ri-cpgi-3*. The indicated area of a multinucleate microspore in (K) is enlarged in (L). Scale bars in (A) to (J) are 10 μm; in (K) and (L) are 5 μm and 2 μm, respectively.

intersporal callose walls of dividing meiocytes so that meiotic cytokinesis was incomplete to form tetrads, which might lead to subsequent pollen degeneration.

The *cpgi-3* knockout mutation likely impaired pre-globular embryo development

The *cpgi* knockout mutants have not been successfully isolated in the progeny of heterozygous *cpgi* mutants (Kunz et al., 2014), which may be due to embryonic lethal. We further examined seed abortion, one of the most common phenotypes caused by embryonic lethality (Meinke and Sussex, 1979; Meinke, 1985; Beeler et al., 2014), in siliques of self-pollinated *cpgi-1*$^{(+/-)}$ and *cpgi-3*$^{(+/-)}$ mutants. In the siliques of 12–14 days after flowering (DAF), we observed that some abnormal seeds looked white, which was easily distinguishable from the normal seeds that looked green

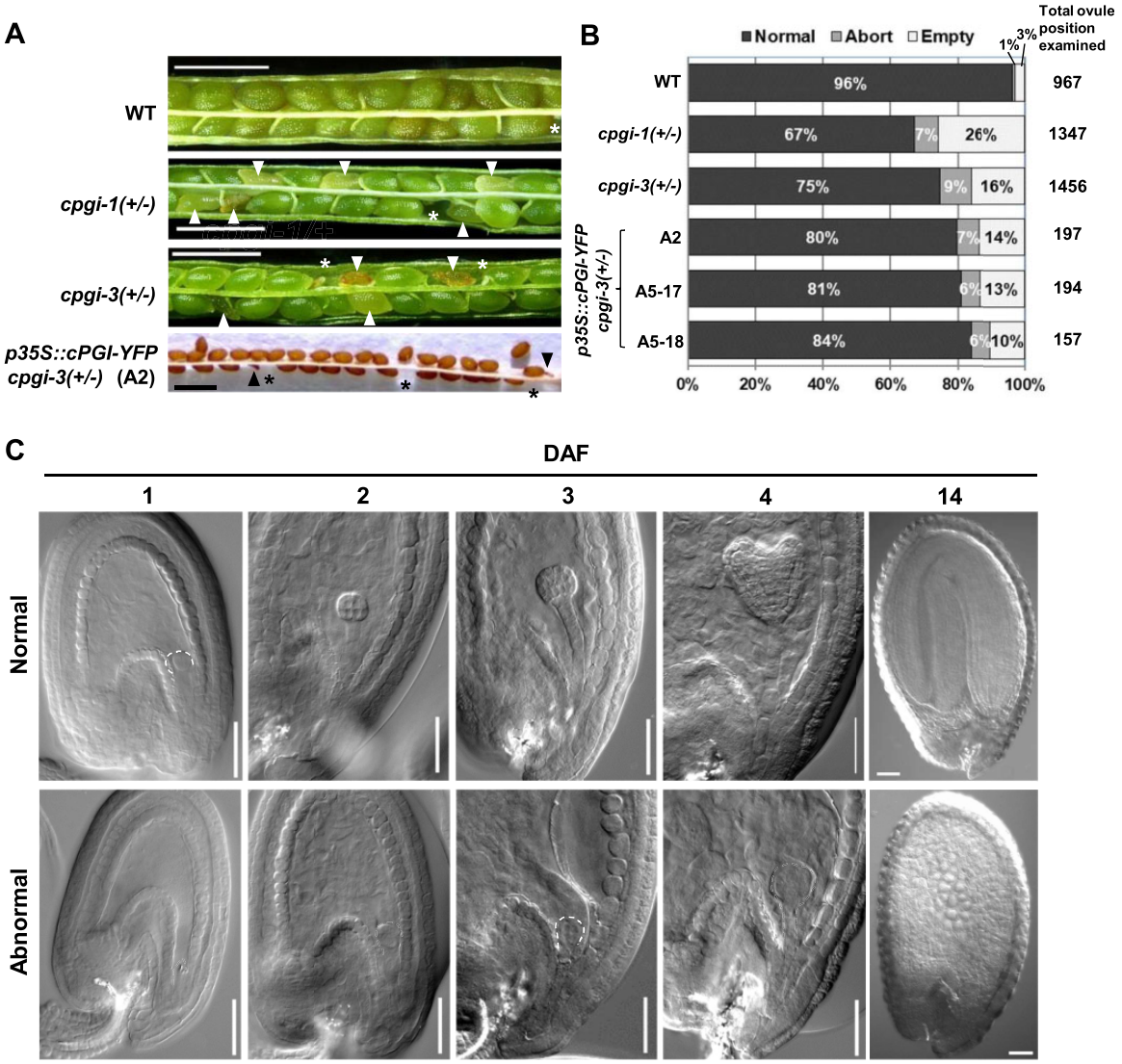

Figure 7 Seed setting and embryo development in the self-pollinated *cpgi-3*$^{(+/-)}$ background plants. A, Seed setting from self-pollination of the indicated plants. Siliques [12–14 DAF for WT, *cpgi-1*$^{(+/-)}$, and *cpgi-3*$^{(+/-)}$; mature siliques for the *p35S::cPGI-YFP cpgi3*$^{(+/-)}$ plants: A2, A5–17, and A5–18] were opened to score the normal seeds (Normal), the aborted seeds (Abort; arrowheads indicated), and the undeveloped seeds as empty spots (Empty; asterisks indicated). An opened silique is shown as a representative. B, Proportions of each type of seeds over the total numbers of ovule position examined are plotted in a 100% stacked bar chart. C, Defective embryo development observed in siliques of *cpgi-3*$^{(+/-)}$ plants. Seeds from young to old (from left to right) siliques corresponding to the indicated DAF were cleared and then inspected by differential interference contrast microscopy for the progression of embryo development. Embryos in the same column showing normal (top) and abnormal (bottom) developmental progression were from the same silique. Note that the abnormal embryos that were undeveloped or likely impaired at the pre-globular stage made up ∼10% of total seeds/ovules inspected. Bars = 50 μm.

(Figure 7A). These white seeds eventually turned brown, collapsed, and aborted in mature siliques (Figure 7A; Supplemental Figure S8). An average of ∼7% and 9% of the total ovule position in each silique of *cpgi-1*$^{(+/-)}$ and *cpgi-3*$^{(+/-)}$ mutants were found to be such aborted seeds (Figure 7B). The proportion of aborted seeds in siliques of *cpgi-1*$^{(+/-)}$ and *cpgi-3*$^{(+/-)}$ mutants was much greater than that in WT plants (∼1%; Figure 7B; Supplemental Table S3). Besides, such seed abortion found in *cpgi*$^{(+/-)}$ siliques was unlikely attributable to gametophytic effects because the resulting aborted seeds from the reciprocal crosses between WT and *cpgi-3*$^{(+/-)}$ mutants were a comparable percentage among total visible seeds harvested (1.3% from *cpgi-3*$^{(+/-)}$♀ × WT♂; 1.5% from WT♀ × *cpgi-3*$^{(+/-)}$♂; 2.1% from WT × WT by hand-pollination; Supplemental Table S3). Therefore, the seed abortion in *cpgi*$^{(+/-)}$ siliques might be mainly attributed to nonviable embryos carrying the homozygous *cpgi* mutation.

In addition to the aborted seeds, a great number of seeds (26% in *cpgi-1*$^{(+/-)}$ and 16% in *cpgi-3*$^{(+/-)}$; Figure 7; Supplemental Table S3) looked undeveloped like nonfertilized or infertile ovules appearing like empty spots in siliques (Figure 7, A and B; Supplemental Table S3), which had also been described in *cpgi-1*$^{(+/-)}$ and *cpgi-2*$^{(+/-)}$ mutants

previously (Kunz et al., 2014). In addition, such abnormalities (aborted seeds and empty spots) were observed in all the examined individuals carrying the *cpgi-3* allele in the progenies of the first and the second backcrosses with the WT, suggesting that the seed defects were genetically linked with the *cpgi-3* allele.

Moreover, we analyzed the seed production in siliques of three *p35S::cPGI-YFP cpgi-3*$^{(+/-)}$ plants, the A2, A5-17, and A5-18 plants. All three plants produced slightly fewer aborted seeds and empty spots (and thus slightly more normal seeds) than the original parental *cpgi-3*$^{(+/-)}$ plants (Figure 7, A and B; Supplemental Table S3). The results might reflect that the *p35S::cPGI-YFP* transgene could only partially complement the *cpgi-3* knockout embryos and thus explain why only a limited number of *p35S::cPGI-YFP cpgi-3*$^{(-/-)}$ plants could be obtained.

To determine at which stage the development of the *cpgi-3* embryo was affected, we inspected chloral hydrate-cleared seeds in siliques harvested at various DAF from the *cpgi-3*$^{(+/-)}$ plants (in the first backcross generation) by differential interference contrast (DIC) microscopy. The embryos in the green seeds developed normally as at the mature embryo stage (Figure 7C, top of the 14 DAF). However, in the aborted white seeds from 14 DAF siliques, we hardly observed any embryo-like structure (Figure 7C, bottom of the 14 DAF). When inspecting a 4 DAF silique, 35 embryos that normally developed to the early heart stage were easily observed (Figure 7C, top of the 4 DAF). In the same silique, other six developing seeds in which embryos developed abnormally as in irregular cell patterning or even unobservable (Figure 7C, bottom of the 4 DAF). Such embryo abnormalities were also observed in each of the 1–3 DAF siliques examined (Figure 7C, bottom), in a similar portion as the aborted seeds found in older/mature siliques (Figure 7, A and B; Supplemental Table S3). In addition, we also observed undeveloped seeds as unfertilized or infertile ovules in each of the 1–4 DAF siliques examined (approximately 10%–20% of total ovules in a silique inspected), which likely ended up with empty spots in mature siliques of *cpgi-3*$^{(+/-)}$ plants. Thus, we concluded that *cpgi* knockout mutation likely impaired the processes of pre-globular embryo development.

A strategy to obtain *cpgi* knockout mutants successfully

A developing embryo is thought to be symplastically isolated from the surrounding endosperm, and the isolation appears at the zygote level (Kozieradzka-Kiszkurno and Płachno, 2012; Sager and Lee, 2014). The embryo acquires primary carbon sources, such as sucrose, glucose, and fructose, mainly from the apoplast by sugar transporters on the plasma membrane (Chen et al., 2015). Since the development of *cpgi-3*$^{(-/-)}$ embryos seem impaired at the pre-globular stage (possibly within 1–2 DAF; Figure 7C), we externally supply sugars (either sucrose, glucose, or fructose) to *cpgi*$^{(+/-)}$ opening flowers (with pollinated pistils) by floral dipping and tried to rescue early embryonic defects of *cpgi-3*$^{(-/-)}$. In a pilot study, seeds harvested from the sugar-fed siliques of *cpgi-3*$^{(+/-)}$ plants were all planted on the soil to screen for *cpgi-3*$^{(-/-)}$ plants. Inspiringly, we isolated a *cpgi-3*$^{(-/-)}$ mutant [*cpgi-3*$^{(-/-)}$ #1] among 150 sibling plants after the 50-mM glucose feeding (Supplemental Table S4). Two more *cpgi-3*$^{(-/-)}$ mutants [*cpgi-3*$^{(-/-)}$ #2 and #3] were isolated among 358 descendants after the 100-mM fructose feeding (Supplemental Table S4). It demonstrated a feasible strategy to obtain *cpgi* knockout mutants, although in a very low frequency (~0.6% isolated in the progeny).

To obtain more *cpgi*$^{(-/-)}$ mutants, we applied the sugar feeding strategy to more flowers and to not only the *cpgi-3*$^{(+/-)}$ but also the *cpgi-1*$^{(+/-)}$ plants. We assumed the sugar-dipping might partially rescue the embryonic defects so that those *cpgi*$^{(-/-)}$ seeds might be underdeveloped. All the seeds harvested from the sugar-fed siliques were visually classified under a dissecting microscope based on seed morphology and size. In addition to the normal and the aborted seeds, some underdeveloped seeds that looked smaller than the normal ones were found (Supplemental Figure S8 and Supplemental Table S5). We firstly checked whether those smaller seeds contain *cpgi*$^{(-/-)}$ mutants. All small and a few normal seeds were sowed on 0.5% Suc-containing plates for germination and growing for 2–3 weeks before transferring them onto soils. Using this strategy, we successfully obtained 24 *cpgi-1*$^{(-/-)}$ mutants (from 88 smaller seeds; Supplemental Table S6) and 47 *cpgi-3*$^{(-/-)}$ mutants (from 278 smaller seeds; Table S6). The *cpgi*$^{(-/-)}$ mutants could be obtained from most of the sugar concentrations tested for feeding except for the 50-mM Glc feeding to *cpgi-3*$^{(+/-)}$ plants [none of *cpgi-3*$^{(-/-)}$ was obtained from only seven smaller seeds; Supplemental Table S6]. If comparing the rescuing rate of *cpgi*$^{(-/-)}$ (% of homozygotes isolated among total sugar-fed seeds harvested), in general, the fructose feeding (0.84%–1.76%) and the sucrose feeding (1.64%–2.1%) were slightly better than the glucose feeding (0%–0.83%; Supplemental Table S6).

Phenotypic analysis of homozygous *cpgi* mutants

Homozygosity of the isolated *cpgi*$^{(-/-)}$ mutants was verified by genomic PCR genotyping (Supplemental Figure S9, A and B). No cPGI in the *cpgi*$^{(-/-)}$ plants was further confirmed by immunoblot analysis and in-gel PGI activity assay (Supplemental Figure S9, C and D). Almost all the *cpgi*$^{(-/-)}$ mutants grew slower than their sibling WT and *cpgi*$^{(+/-)}$ plants in the young vegetative phase, even growing on Suc-containing media (Figure 8A). After transferring to the soil, many *cpgi*$^{(-/-)}$ mutants still grew relatively slowly although few of them grew as similarly as their WT and *cpgi*$^{(+/-)}$ sibling plants did (Figure 8B). In most cases, the *cpgi*$^{(-/-)}$ mutants was relatively smaller than their same-aged WT and *cpgi*$^{(+/-)}$ siblings. However, some were capable of growing as large as the WT, but it took a longer time (Figure 8B), implying that such plant size-related phenotypes might not be solely attributed to the *cpgi* knockout mutation. The *cpgi-1*$^{(-/-)}$ and *cpgi-3*$^{(-/-)}$ mutants exhibited starch-excess phenotypes in leaves (Figure 8C), similar to the *Ri-cpgi* lines

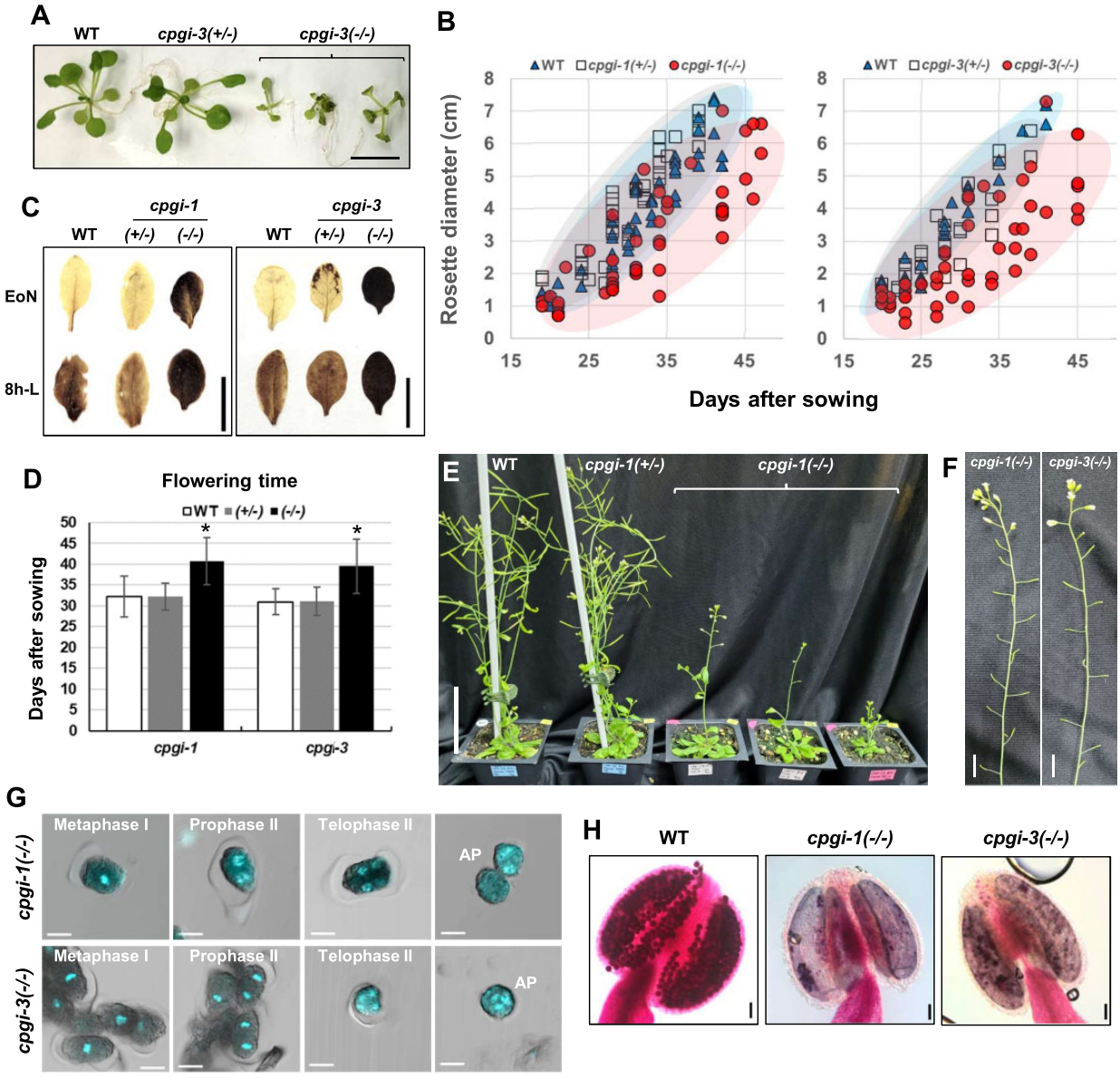

Figure 8 Phenotypes of the rescued *cpgi* knockout mutants. A, Seeds harvested from the sugar-fed siliques of *cpgi*$^{(+/-)}$ plants were planted on half-strength Murashige and Skoog media containing 0.5% Suc for screening for *cpgi*$^{(-/-)}$ mutants. Here, as indicated, five representative 25-day-old siblings were photographed before the genotypic identification of *cpgi-3* zygosity, showing a diminished young vegetative growth in *cpgi-3*$^{(-/-)}$ plants. Bar = 1 cm. B, After transferring the seedlings from plate to soil, rosette diameter (cm) of the individual plant was scored through time and plotted to demonstrate vegetative growth of WT, *cpgi*$^{(+/-)}$, and *cpgi*$^{(-/-)}$ plants. C, Iodine staining for starch content in leaves. The *cpgi-1*$^{(-/-)}$ and *cpgi-3*$^{(-/-)}$ plants exhibited starch-excess phenotypes. Bars = 1 cm. D, Flowering time of WT, *cpgi*$^{(+/-)}$, and *cpgi*$^{(-/-)}$ plants. Day after sowing mean ± SD is shown (n = 10–18). *Significantly different from WT (t test; $P < 0.001$). E, Representative plants were photographed 45 days after sowing to demonstrate late flowering in *cpgi-1*$^{(-/-)}$ plants. Bar = 5 cm. F, All the *cpgi-1*$^{(-/-)}$ and *cpgi-3*$^{(-/-)}$ plants were completely sterile and representative inflorescence stems are shown. Bars = 1 cm. G, DAPI staining to demonstrate the impaired progression of microsporogenesis in *cpgi-1*$^{(-/-)}$ and *cpgi-3*$^{(-/-)}$ plants, which was similar to the phenotypes of defective formation of intersporal callose wall observed in *Ri-cpgi-3* (Figure 6). Merged confocal micrographs (DAPI/DIC) are shown. Meiotic stages were determined from the DAPI-stained morphology. Abnormal pollen (AP) looked like the outer callose wall-dissolved meiocytes. Bars = 10 μm. H, Alexander staining for pollen viability. Bars = 50 μm.

(Figure 3A). The transition to flowering was delayed in *cpgi-1*$^{(-/-)}$ and *cpgi-3*$^{(-/-)}$ mutants (Figure 8, D and E), probably attributed to the slow growth in young vegetative phase (Figure 8B). In contrast to the great individual variance in vegetative growth, the complete sterility was consistent in all the isolated *cpgi-1*$^{(-/-)}$ and *cpgi-3*$^{(-/-)}$ plants (Figure 8, F–H) due to the similar defective progression of microsporogenesis found in *Ri-cpgi-3* plants (Figure 6), that is impaired formation of intersporal callose wall (Figure 8G), whose defects led to pollen degeneration (Figure 8H) and thus male sterility.

We further tested for female fertility in *cpgi-1*$^{(-/-)}$ and *cpgi-3*$^{(-/-)}$ mutants by pollinating pistils with pollen grains from either the WT or the *cpgi*$^{(+/-)}$ plants (Figure 9). These

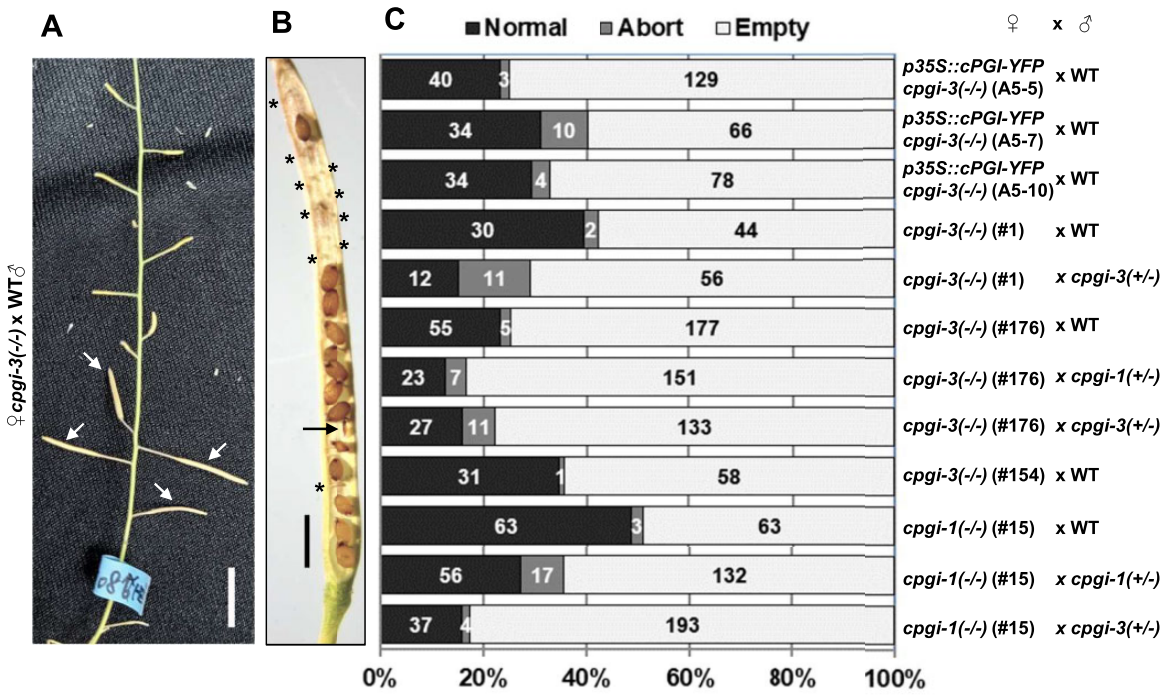

Figure 9 Loss of cPGI greatly impaired female fertility. A, Resulting siliques (arrowhead indicated) from manually pollinating a *cpgi-3*$^{(-/-)}$ plant with pollen grains from WT plants. Bar = 1 cm. B, Mature siliques were opened to score the seed setting from the manual pollinations. An opened silique from the *cpgi-3*$^{(-/-)}$ (#176) × WT is shown as a representative. The aborted seeds (arrow) and the empty spots (asterisks) are indicated. Bar = 1 mm. C, Quantification data of detailed numbers of each type of seed scored from the resulting siliques of the indicated manual pollinations are plotted in a 100% stacked bar chart.

crosses led to elongated siliques (Figure 9A), but approximately 20%–50% ovules were fertilized to set seeds (Figure 9, B and C; Supplemental Table S3), indicating greatly impaired female fertility. Similar impaired female fertility was also found in three independent *p35S::cPGI-YFP cpgi-3*$^{(-/-)}$ plants (A5-5, A5-7, and A5-10) by evaluating the seed set after pollinating with WT pollen (Figure 9, B and C). The results suggested that the impaired female fertility of *cpgi-3*$^{(-/-)}$ background could not be remedied metabolically by neighboring cells or source tissues expressing functional cPGI-YFP fusion proteins.

Discussion

The functions of cPGI in the tapetum and microsporocytes are crucial for microsporogenesis

In this study, we investigated different cPGI-deficient Arabidopsis lines, *cPGI*-knockdown (*Ri-cpgi* and *cPGI-co* lines), *cPGI*-knockout (the rescued *cpgi-1* and *cpgi-3* mutants), and the partially complemented line *p35S::cPGI-YFP cpgi-3*$^{(-/-)}$. Almost all lines showed that cPGI-deficiency were associated with male infertility, except for the *Ri-cpgi-10* line (Figures 1 and 3, B). The three *Ri-cpgi* lines examined and the *cpgi* knockout mutants all exhibited starch-excess phenotypes (Figures 3, A and 8, C), which were highly associated with cPGI deficiency in leaves (Figure 3, C and D). The altered starch metabolism did not impact the male fertility of the *Ri-cpgi-10* line (Figures 1 and 3, B). Similarly, reduced fertility has not been reported in other starch-excess mutants defective in transitory starch degradation, such as *sex1*, *sex4*, and *lsf1* (Yu et al., 2001; Kötting et al., 2009; Comparot-Moss et al., 2010), implying that altered starch metabolism in the source leaves might not be the primary cause of the male sterility induced by cPGI deficiency.

In contrast, the severity of male infertility in *Ri-cpgi* lines seemed highly associated with the strength of cPGI suppression in developing floral buds and the defects in intersporal callose wall formation. Complete loss of cPGI in the rescued *cpgi* mutants was associated with completely male sterility. Such association suggests that cPGI function (most likely its enzyme activity) is required for the formation of intersporal callose wall in a meiocyte to complete microsporogenesis and to subsequently develop into viable pollen. Moreover, the completely male sterile *p35S::cPGI-YFP cpgi-3*$^{(-/-)}$ plants provided a special cPGI deficiency in those tissues where the *p35S* promoter was inactive. Although the *p35S* has been considered a constitutive promoter, some studies indicate it is not active during pollen development and early embryogenesis (Wilkinson et al., 1997; Custers et al., 1999; Sunilkumar et al., 2002). Recently, a study reported that the *p35S* promoter is active in the epidermis and endothecium but not active in the middle layer, tapetum, or microspores in anthers (Xue et al., 2021), which supports our

interpretation that the loss of cPGI restrictedly in the tapetum and pollen would sufficiently abolish the formation of a tetrad. Our data further suggest that such anther defects cannot be remedied metabolically by the adjacent cells or the source tissues containing the functional cPGI-YFP in the *p35S::cPGI-YFP cpgi-3*$^{(-/-)}$ plants.

Tapetal cells provide nutrients, enzymes, and precursors for pollen growth (Ma, 2005; Slewinski, 2011). Therefore, disrupting tapetal function usually results in pollen defects that cause male sterility (Zhang et al., 2006; Zhu et al., 2008). Since the male sterility induced by cPGI deficiency can result from dysfunction of either the tapetum or pollen per se or from miscoordination between the tapetum and pollen, it is still an open question and needs to be further clarified the contributions of cPGI function from the tapetum or in pollen to the intersproal callose wall formation. To express either tapetum-specific or meiocyte-specific *cPGI-YFP* in the *cpgi* knockout mutant may have great potential to answer this question.

cPGI may be required for regulating carbohydrate partition in symplastically isolated meiocytes

Our results suggest that the defects in intersporal callose wall formation in the different cPGI-deficient lines are unlikely to be attributed to the altered expression of key genes related to callose metabolism during microsporogenesis. Another possible explanation of the defects in intersporal callose wall formation would be the insufficient provision of UDP-Glc for callose synthesis during the critical stage of late male meiosis in the strongly cPGI-repressed lines and *cpgi* knockout plants. In plant cells, several enzyme-mediated reactions can potentially generate UDP-Glc, including UDP-Glc pyrophosphorylase (UGPase), UDP-sugar pyrophosphorylase (USPase), and sucrose synthase (SuSy; Park et al., 2010; Kleczkowski et al., 2011). UGPase and USPase catalyze the same reversible conversion of glucose-1-phosphate (G1P) and UTP to UDP-Glc and pyrophosphate. SuSy catalyzes the reversible conversion of sucrose and UDP to fructose and UDP-Glc. No defect in fertility is reported in the Arabidopsis mutants lacking the four major isoforms of SuSy (Barratt et al., 2009). The loss of UGPase, however, impairs pollen callose deposition and results in male sterility in Arabidopsis and rice, suggesting either SuSy or USPase could not compensate for the *ugp* mutation (Chen et al., 2007; Park et al., 2010). These lines of genetic evidence suggest the UGPase-mediated G1P to UDP-Glc conversion is the main flux for callose deposition in Arabidopsis male meiocytes. The cytosolic hexose phosphate pool, consisting of G1P, G6P, and F6P, is maintained in equilibrium by cytosolic phosphoglucomutase (cPGM) and cPGI to supply to various cellular metabolisms (Kunz et al., 2014; Malinova et al., 2014). It has been reported that lacking cPGM activity also affects pollen viability and seed production (Egli et al., 2010; Malinova et al., 2014). Thus, the substrate UDP-Glc required for callose deposition in male meiocytes to form tetrads is mainly derived from the hexose phosphate pool.

We propose a model to interpret the indispensability of cPGI function in synthesizing intersporal callose wall of Arabidopsis microsporocytes (Figure 10). Sucrose (Suc), the main transported carbohydrates, can be unloaded and transported apoplastically or symplastically (through plasmodesmata) to the fast-growing sinks in young anthers, the tapetum and the PMCs. Suc can be imported directly into a PMC or be converted into Glc and Fru by cell-wall invertase (cw-INV) at the apoplast and then Glc and Fru can be taken up by sink-specific sugar transporters at the plasma membrane (Lemoine et al., 2013; Rottmann et al., 2018). The hexoses in the cytosol, from being imported or from Suc hydrolysis by cytosolic INV (INV), are then phosphorylated by hexokinase (HXK) or fructokinase (FRK) into G6P and F6P to enter cellular metabolism. The male meiosis is accompanied by the deposition of callose in between the primary cell wall and plasma membrane of the PMC (becoming an outer callose wall-encased meiocyte), and it finishes after the formation of the intersporal callose wall to separate the four haploid daughter nuclei (forming a tetrad microspore). The outer callose wall blocks the plasmodesmata connecting microsporocyte to microsporocyte and microsporocyte to tapetum (Owen and Makaroff, 1995; Sager and Lee, 2014), making the microsporocytes symplastically isolated (Engelke et al., 2010; Slewinski, 2011; Sager and Lee, 2014). In addition, callose has been considered as a permeability barrier (Stone, 2009) and may restrict solutes but not water movement (Yim and Bradford, 1998). Thus, sugar import into a meiocyte might become relatively restricted after the outer callose wall formed. On the other hand, the meiotic progression from a diploid meiocyte to the segregation of four haploid nuclei into a tetrad is estimated to be achieved within three hours in Arabidopsis (Armstrong et al., 2003). As meiosis synchrony occurs in anther locules, the demand of UDP-Glc for callose deposition must be high. Such limitation of available sugars in a meiocyte makes the cPGI-dependent carbohydrate partition indispensable for efficiently metabolizing F6P–G6P conversion toward the high demand of UDP-Glc substrate for synthesizing intersporal callose wall at the final step of completing male meiosis. This proposed model may explain the similar phenotypes of defective formation of intersporal callose wall in meiocytes found in different cPGI-deficient lines [strong *cPGI*-knockdown lines, *p35S::cPGI-YFP cpgi-3*$^{(-/-)}$ plants, and the rescued *cpgi* knockout mutants].

The loss of cPGI in haploid pollen does not affect microgametogenesis but reduces gametophyte transmission

Our study showed that the *cpgi-3*$^{(+/-)}$ mutants produced similar amounts of viable pollen as the WT did (Figure 1B), and they could transmit the *cpgi-3* lesion to the next generation through pollen. This indicates that the microspores carrying the disrupted *cPGI* gene could develop normally to viable pollen with the support of the tapetum and other sporophytic cells carrying the WT *cPGI* allele, as the *cpgi*

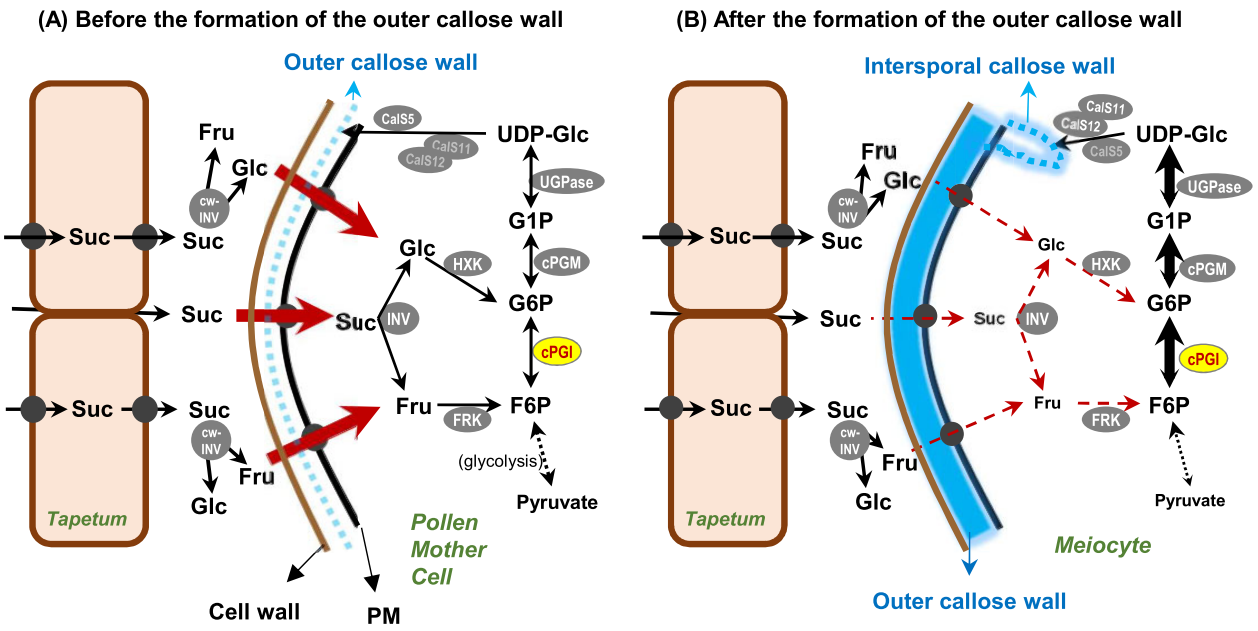

Figure 10 A proposed model of cPGI function in Arabidopsis microsporogenesis. Sucrose (Suc), the main transported form of photosynthate from the source, can be unloaded and transported apoplastically or symplastically (through plasmodesmata) to the fast-growing sink in young anthers, the tapetum and PMCs. Suc can be imported directly into a PMC or be converted into Glc and Fru by cell-wall invertase (cw-INV) at the apoplast, and then those sugars can be taken up by sink-specific sugar transporters (solid black circle) at the plasma membrane. The hexoses in the cytosol, either imported or from Suc hydrolysis by cytosolic INV (INV), are then phosphorylated by hexokinase (HXK) or fructokinase (FRK) into G6P and F6P to enter cellular metabolism. Male meiosis is accompanied by the deposition of callose in between the primary cell wall and plasma membrane of the PMC (becoming an outer callose wall-encased meiocyte), and is complete after the formation of the intersporal callose wall to separate the four haploid daughter nuclei (forming a tetrad microspore). Callose (β-1,3-glucan) is synthesized by callose synthases (CalS) using the glucose residue of UDP-glucose (UDP-Glc), which is mainly derived from the G6P–G1P route. The formation of the outer callose wall may block the symplastic route of sugar diffusion between tapetum and meiocyte (as well as between two meiocytes), and thus sugar import into a meiocyte becomes relatively restricted. Such limitation of available sugars in a meiocyte makes the cPGI-dependent carbohydrate partition indispensable for efficiently metabolizing the F6P–G6P conversion toward the high demand of UDP-Glc synthesis for the formation of intersporal callose wall at the final step of completing male meiosis. cPGM, cytosolic phosphoglucomutase; UGPase, UDP-glucose pyrophosphorylase.

lesion segregates after male meiosis. Thus, the loss of cPGI in pollen during microgametogenesis seems to have little impact on its maturation and viability.

However, in this study, the much less than the expected *p35S::cPGI-YFP cpgi-3*$^{(-/-)}$ plants were isolated from the progeny of crossing the *p35S::cPGI-YFP* plants with *cpgi-3*$^{(+/-)}$ or *p35S::cPGI-YFP cpgi-3*$^{(+/-)}$ with *cpgi-3*$^{(+/-)}$. The analysis of reciprocal crosses between WT and *cpgi-3*$^{(+/-)}$ indicated that a reduced transmission efficiency through the male (62% WT efficiency) and female gametophytes (79% WT efficiency) carrying the *cpgi-3* lesion was found as evaluated by reciprocal cross-analysis (Supplemental Table S2). Such reduced gametophytic transmission is also reported in the *cpgi-1* and *cpgi-2* mutants (Kunz et al., 2014). A fast-growing pollen tube, another symplastic isolated sink cell type, synthesizes callose plugs inside the pollen tube and deposits callose along the pollen tube wall except in the tip zone (Li et al., 2020). It is also highly metabolically active that requires efficient partitioning of nutrients, for which cPGI might play a crucial role. The reduced transmission efficiency might be caused by the less competitive capacity of *cpgi* pollen than WT pollen during the pollination and fertilization processes. Further investigation is needed to clarify this postulation.

cPGI-mediated carbohydrate partitioning is crucial for early embryogenesis

UDP-Glc is a substrate for synthesizing cell wall components, not only callose but also cellulose (β-1,4 glucan). Embryo development involves serial processes of cell division and cell expansion, which is relied on nutrients provided by maternal sources. Similar to developing pollen and pollen tubes, a developing embryo is thought to be symplastically isolated from the surrounding endosperm, and the isolation appears at the zygote level (Kozieradzka-Kiszkurno and Płachno, 2012; Sager and Lee, 2014). Our results suggest that efficient carbohydrate partitioning mediated by cPGI is indispensable for early embryogenesis. Using a strategy combining external feeding of sugars to the heterozygous *cpgi* mutants by floral dipping and growing those resulting seeds on sucrose-containing media can rescue the lethality of *cpgi* knockout mutation, although the likelihood is still small (Supplemental Tables S4 and S5; Figure 8). Our data also imply that once the critical stage of cPGI deficiency is

overcome, perhaps by the sugar feeding, the progression of *cpgi* embryogenesis can be accomplished. It is still an open question whether the sugars serve as nutrient supplements to fuel the hexose phosphate pool directly or as signaling molecules that activate other metabolic pathways to compensate for the loss of cPGI function during early embryogenesis. In addition, the female fertility of rescued *cpgi* knockout mutants is greatly impaired but not fully abolished (Figure 9), suggesting the cPGI-mediated carbohydrate partition in megagemetophytic development is not as indispensable as that in microsporogenesis. Further investigation is needed to address these questions.

Conclusion

Based on the similar defects of impaired microsporogenesis resulting from different cPGI-deficient lines, we propose that cPGI-mediated carbohydrate partition is indispensable for synthesizing the intersporal callose wall in a meiocyte to form a tetrad, which is an essential process in microsporogenesis and for producing viable pollen. The cPGI function is also indispensable for young embryogenesis because no viable *cpgi* homozygous mutants could be obtained under conventional conditions, but the external supply of sugars might alleviate such cPGI indispensability to produce viable *cpgi* seeds. Additionally, the female fertility of rescued *cpgi* knockout mutants was greatly impaired but not fully abolished, suggesting the cPGI-mediated carbohydrate partition in megagemetophytic development is not as indispensable as that in microsporogenesis.

Materials and methods

Plant materials and growth conditions

The Arabidopsis (*Arabidopsis thaliana*) *cpgi-1* (Salk_064423) mutant seeds were obtained from the Arabidopsis Biological Resource Center (https://abrc.osu.edu/). The *cpgi-3* seeds, a set of T3 seeds of the GABI-Kat mutant line GK-013D09 (Kleinboelting et al., 2012), were obtained from the Nottingham Arabidopsis Stock Center (Scholl et al., 2000). The WT background used to generate the *Ri-cpgi* transgenic lines was the Col-5 (Stock No. CS1688). Plants were grown on soil in a growth chamber under the following conditions unless otherwise stated: 100 μmol photons m^{-2} s^{-1}, 16-h light/8-h dark regimes, 24°C ± 2°C.

Plasmid construction

For the *p35S::RNAi-cPGI* construct, nucleotides +1397 to +1680 of the Arabidopsis *cPGI* (At5g42740) coding sequence were amplified from RT-generated leaf cDNA with primers p1188 and p1189 (Supplemental Table S7) using *Pfu*-Taq DNA polymerase. After subcloning into the pZErO-2.1 vector (Invitrogen) following the manufactory's instruction and sequencing, the *cPGI* fragments (~300 bp), separately generated by AscI–SwaI and BamHI–XbaI double digestions, were directionally introduced into the binary vector pFGC5941 (Kerschen et al., 2004) using the corresponding restriction sites for inverted orientations flanking, respectively, at 5′- and 3′-ends of an intron from the *Petunia hybrida* Chalcone synthase A gene to generate the *p35S::RNAi-cPGI* construct.

For the cPGI-YFP fusion construct, the *cPGI* open reading frame (without the stop codon) was amplified from Arabidopsis leaf cDNA using high-fidelity *Pfu*-Taq DNA polymerase with primers pS009 and pS010 (Supplemental Table S7) to incorporate AscI and SwaI restriction sites at the 5′- and 3′-prime end, respectively, and then ligated into the AscI–SwaI linearized *p53AS-eYFP3* binary vector (derived from pPZP221 in Dr Chen lab) for the translational fusion of YFP to the C-terminal end of cPGI. The coding region of *cPGI* in the generated *p35S::cPGI-YFP* fusion construct was sequenced and shown to be identical to that of a *cPGI* cDNA clone (Genebank ID: AF372970) but was different from the annotated *At5g42740.1* by TAIR with a single nucleotide difference at position +647, which leads to Phe216Ser amino acid difference. We thought this might reflect an unidentified single nucleotide polymorphism of *cPGI* in Arabidopsis, so we kept using this construct in this study.

Generating the stably transformed Arabidopsis

Plasmid constructs were transferred into *Agrobacterium tumefaciens* GV3101 using the freeze–thaw method (Höfgen and Willmitzer, 1988), and the bacteria were used to transform WT plants using the floral dip method (Clough and Bent, 1998). Seeds were collected from the transformed plants and were then screened with appropriate antibiotics or herbicides (Basta for *Ri-cpgi* and *p35S::cPGI-YFP* transgenic plants). Resistant seedlings were selected as candidates and were further verified by genomic PCR genotyping, immunoblot analysis, or in-gel PGI activity assay.

Isolation of *Ri-cpgi* mutant lines

Several independent *Ri-cpgi* transformants were isolated by screening for Basta herbicide resistance. In the T3 generation of the *Ri-cpgi-1* family, two sibling plants, *Ri-cpgi-1.1.3* and *Ri-cpgi-1.1.4*, were found to produce many seedless siliques, which were different from other Basta-resistant siblings that produced elongated siliques (such as the *Ri-cpgi-10* line used here; Figure 1). Along with the seedless siliques, some elongated siliques containing viable seeds were produced in both *Ri-cpgi-1.1.3* and *Ri-cpgi-1.1.4* plants. After pollinating with WT pollen, the resulting siliques of both plants were elongated to set seeds. The progenies of *Ri-cpgi-1.1.3* and *Ri-cpgi-1.1.4* self-pollination and of the backcrossing with WT all exhibited homogenous Basta resistance, suggesting homozygosity of the *Ri-cpgi-1* transgenic alleles. Thus, the descendants of the *Ri-cpgi-1.1.4* line were selected to represent the *Ri-cpgi-1* line for further phenotypic analysis.

Similarly, we isolated a *Ri-cpgi-10* line from the selfed progeny of a parental plant which exhibited a Basta-resistant phenotype with a segregation ratio close to 3:1. In contrast to the *Ri-cpgi-1* line showing reduced male fertility, the *Ri-cpgi-10* line was fertile. Regarding the *Ri-cpgi-3* line, interestingly, the progenies propagated from the few viable seeds produced in this line displaying male sterility always

contained some Basta-sensitive descendants, suggesting heterozygosity for the *Ri-cpgi-3* allele. We did not isolate any probable homozygotes yet. Thus the Basta-resistant descendants of *Ri-cpgi-3* exhibiting male sterility were used as representatives for subsequent phenotypic analyses.

Generation of the *p35S::cPGI-YFP cpgi-3*$^{(-/-)}$ plants

To generate the *p35S::cPGI-YFP cpgi-3*$^{(-/-)}$ plants, we crossed the heterozygous *cpgi-3*$^{(+/-)}$ plants with the *cPGI-ox* transformants (T1) which was possible with a single transgenic allele of *p35S::cPGI-YFP* as their T2 progenies exhibited Basta resistance in a segregation ratio close to 3:1. Then the F1 progenies were screened for harboring both the transgenic alleles of *cpgi-3* and *p35S::cPGI-YFP* by combining Sul and Basta selection. In the F2 generation, plants were screened first for Sul resistance, followed by Basta selection (for segregation analysis shown in Supplemental Table S1). Homozygosity of the *cpgi-3* T-DNA allele was confirmed by genomic PCR genotyping. Expression of the *p35S::cPGI-YFP* was further confirmed by examining the YFP fluorescence in tissues, immunoblot analysis, or in-gel PGI activity assay.

Protein methods

For the in-gel PGI activity assay, soluble proteins were extracted from plant tissues with extraction buffer (0.1-M Tris–HCl, pH 7.5, 0.1-M KCl, 10-mM $MgCl_2$, 40-mM β-mercaptoethanol, 15% (v/v) glycerol; using 2 μL mg^{-1} for the extraction of fresh leaf tissues or 4 μL mg^{-1} for extraction of floral buds) and clarified by centrifugation at 4°C, 15,000*g* for 5 min. Crude protein extracts (10 μL) were subjected to 7.5% nondenaturing polyacrylamide gel for PGI activity assay on the native gel as described previously (Yu et al., 2000). Briefly, the native gel was incubated in 10 mL of reaction solution [0.1-M Tris–HCl, pH 7.0, 10-mM $MgCl_2$, 4.3-mM F6P, 130-μM $NADP^+$, 8 units of G6P dehydrogenase (G6PDH); 8 μg/mL^{-1} phenazine methosulfate; 0.2 mg/mL^{-1} thiazolyl blue tetrazolium bromide] at 37°C until the blue–purple bands of fomazan precipitation clearly appeared on the gel area where there contains PGI enzyme activity to convert F6P to G6P for the G6PDH–NADPH-coupled reaction. To visualize the YFP signals of the cPGI–YFP fusion protein, the same gel after the in-gel PGI activity assay was scanned by using the Typhoon Trio Imager (GE Healthcare) with the fluorescence emission filter 520DBP40 (for emission wavelength 500–540 nm; Supplemental Figure S1E).

For immunoblot analysis, the crude protein extracts were subjected to 10% SDS–polyacrylamide gel electrophoresis (Supplemental Figure S1D) or NuPAGE 4%–12% Bis–Tris gel electrophoresis (Figure 3D) and then transferred onto a polyvinylidene fluoride (PVDF) membrane. Rabbit antisera were raised using purified, *Escherichia coli*-expressed recombinant Arabidopsis cPGI proteins as antigens. The antisera (1:1,000) were used in combination with horseradish peroxidase (HRP)-conjugated goat anti-rabbit IgG secondary antibody (1:2,000; Thermo Fisher Scientific) and Lumi-Light Western Blotting Substrate (Sigma-Aldrich) for the immunoblot analysis. Anti-tubulin antibody was purchased from Merck Millipore (Cat. No. AB3203). ImageJ (https://imagej.nih.gov/) was used to quantify the relative amount of bands in gels or on immunoblots (Figure 3, C and D).

Cytology and microscopy

Inspection of embryos in developing seeds was as described previously (Beeler et al., 2014). Briefly, siliques containing developing seeds were harvested and then cleared with chloral hydrate clearing solution (40-g chloral hydrate, 15-mL water, and 5-mL glycerol) overnight at room temperature. The cleared seeds were inspected using DIC microscopy. Pollen viability was assessed by Alexander staining (Alexander, 1969). For cross-sections of anthers, unopened flower buds were fixed in 2.5% (v/v) glutaraldehyde and 4% (v/v) paraformaldehyde in 0.1-M sodium phosphate buffer, pH 7.0 at room temperature for 4 h. After rinsing with buffer three times for 20 min, the samples were postfixed in 1% (w/v) OsO_4 in the same buffer for another 4 h followed by rinsing with buffer another three times. After dehydration in an acetone series, the samples were embedded in LR White resin and were sectioned with a Leica Reichert Ultracut S or Leica EM UC6 ultramicrotome. Semi-thin cross-sections (0.8–1 μm) were stained with 1% (w/v) toluidine blue. Micrographs of the sections were taken by Zeiss Imager Z1 microscope equipped with AxioCam HRc digital camera and AxioVision Rel. 4.8 software. Ultrathin cross-sections (70–90 nm) were stained with 5% (w/v) uranyl acetate in 50% (v/v) methanol for 10 min and followed by 0.4% (w/v) lead citrate for 4 min. Sections were observed using an FEI Tecnai Spirit G20 Transmission Electron Microscope at 80 KV, and images were acquired by Gatan Orius CCD camera.

The method to visualize callose walls of microsporocytes and tetrad microspores using aniline blue staining was slightly modified from Mori et al. (2006). Inflorescence apices containing floral buds in various sizes were fixed in acetic acid: ethanol (1:3; v/v) fixative at 4°C in the dark overnight. The fixed buds were rehydrated by ethanol series (70%, 50%, and 30%) for at least 10 min for each step and finally by double-distilled water. The samples were transferred to the aniline blue staining solution [0.01% (w/v) aniline blue (Applichem, product code:253708) in 50-mM K_2HPO_4] and stained at 4°C in the dark overnight. After measuring the bud size under a dissecting microscope, the anthers were dissected carefully from the floral bud in a drop of the staining solution and then mounted on glass slides with coverslips for confocal microscopy imaging. The Zeiss LSM780 system was used to image aniline blue-callose fluorescence with 405-nm laser (5% intensity) for excitation, 410–490 nm bandwidth for the signal collection, and setting 600–680 for the master gain.

The DAPI staining was used to examine male meiotic nuclear division (Liu et al., 2014). Anthers were dissected from the acetic acid: ethanol fixed floral buds and mounted on microscope slides with a drop of DAPI staining solution (2 μg mL^{-1}). Microsporocytes were released from the anther locules by gently pressing the coverslip of the mounted slide and then examined by confocal microscopy using the same

settings for imaging the aniline blue-callose fluorescence as above mentioned.

Analysis of cPGI expression using publicly accessible transcriptome datasets

Expression data of the *cPGI* (At5g42740) and the reference gene *ACTIN 8* (*ACT8*; At1g49240) were obtained from the Arabidopsis eFP Browser (http://bar.utoronto.ca/efp_arabidopsis/cgi-bin/efpWeb.cgi; Winter et al., 2007) compiled transcriptome datasets (Honys and Twell, 2004; Klepikova et al., 2016; Li et al., 2017; Hofmann et al., 2019). The tapetum-specific RNA-seq data were obtained from Li et al. (2017) and then processed according to Huang and Suen (2021). To evaluate the relative expression between tissues, the *cPGI* transcript levels were normalized to those of the reference gene *ACT8* and shown in the ratio *cPGI*/*ACT8* (Supplemental Figure S1, A–D).

RT–qPCR analysis

Anthers were collected from 0.5-mm to 0.8-mm buds and then combined for total RNA extraction using the GeneMark plant total RNA purification kit (GMbiolab, Taiwan). After DNase treatment (TURBO DNA-*free* kit, Invitrogen) to eliminate trace DNA contaminations, 1.8-μg RNA was reverse transcribed using the Superscript III First-Strand Synthesis System (Invitrogen) with oligo-dT primers. The reverse transcribed products (400 ng) were used as the template for RT–qPCR analysis using gene-specific primers listed in Supplemental Table S7 and the ABI 7500 Fast Real-Time PCR System.

Feeding *cpgi*$^{(+/-)}$ flowers with sugar solutions for rescuing embryos with *cpgi* knockout mutation

Before floral dipping, developing siliques on inflorescence stems were removed. The remaining inflorescence apex (containing developing floral buds) along with newly opening flowers (with self-pollinated pistils <2 DAF) on a stalk was dipped into one of the following solutions for each stalk: mock solution (0.02% (v/v) Silwet L-77; Helena Chemical Company), sucrose (50 mM, 100 mM, or 150 mM), glucose (50 or 100 mM), or fructose (50 or 100 mM) solution. All the sugar solutions were prepared in the mock solution. Each stalk was dipped for 10–20 s and then labeled accordingly. The sugar feeding was done once a day for one to three replicated dipping afterward for more sugar-fed siliques. Seeds were harvested upon maturation for screening for *cpgi* knockout mutants in the progeny.

In a pilot study, seeds harvested from the sugar-fed siliques of *cpgi-3*$^{(+/-)}$ plants were all planted on soil to screen for plants resistant to sulfadiazine foliar selection (Thomson et al., 2011), which would include *cpgi-3*$^{(+/-)}$ and the rescued *cpgi-3*$^{(-/-)}$ mutants. To obtain more *cpgi*$^{(-/-)}$ mutants, we applied the sugar feeding strategy to more opening flowers of not only the *cpgi-3*$^{(+/-)}$ but also the *cpgi-1*$^{(+/-)}$ plants. After dipping, the pistil (with pollen grains on the stigma) soaking in a drop of sugar solution was confirmed under a dissecting microscope. The sugar-fed flowers were labeled accordingly. The seeds produced within the sugar-fed siliques were harvested upon maturation. The harvested seeds were visually classified into three groups based on seed morphology and size (please see Supplemental Figure S8 for the image). Selected seeds (mainly the smaller seeds) were planted on half-strength Murashige and Skoog, 0.5% (w/v) Suc plate for germination and growth for 2–3 weeks then the survivals were transferred onto soil for further growth.

Statistical analysis

The data are subjected to Student's *t* test for statistically significant difference ($P < 0.05$). Results are shown as mean ± SD or mean ± SE as indicated.

Accession numbers

Sequence data from this article can be found in the GenBank/EMBL data libraries under accession numbers: At5g42740 (cPGI), At1g49240 (ACT8), At3g24330 (a putative callase), At2g13680 (CalS5/GSL2), At4g04970 (CalS11/GSL1), At4g03550 (CalS12/GSL5), At4g24620 (PGI1).

Supplemental data

The following materials are available in the online version of this article.

Supplemental Figure S1. Verification of the *p35S::cPGI-YFP cpgi-3*$^{(-/-)}$ and *cPGI* co-suppressed (*cPGI-co*) plants.

Supplemental Figure S2. Distribution of YFP fluorescence in developing anthers of the completely male-sterile *p35S::cPGI-YFP cpgi-3*$^{(-/-)}$ plant.

Supplemental Figure S3. Expression of *cPGI* (At5g42740) in Arabidopsis.

Supplemental Figure S4. Phenotypic characterization of *Ri-cpgi* lines.

Supplemental Figure S5. Loss of cPGI did not dramatically impair the development of floral organs.

Supplemental Figure S6. Aniline blue staining for callose contents in whole-mount anthers.

Supplemental Figure S7. RT–qPCR analysis of the selected genes related to callose metabolism during pollen development in the *Ri-cpgi* lines.

Supplemental Figure S8. Seeds from the sugar-fed *cpgi-3*$^{(+/-)}$ siliques.

Supplemental Figure S9. Verification of the rescued *cpgi* knockout mutants.

Supplemental Table S1. Segregation analysis of the *p35S::cPGI-YFP cpgi-3*$^{(+/-)}$ plants.

Supplemental Table S2. Analysis of the genetic transmission of the *cpgi-3* allele, as determined by sulfadiazine resistance (Sul^{R}) in the selfed progeny of heterozygous *cpgi-3*$^{(+/-)}$ and in the progenies of reciprocal crosses with the WT.

Supplemental Table S3. The number of three morphological types of seeds in siliques from self-pollination and from the crosses between the indicated plants.

Supplemental Table S4. A feasibility attempt to obtain *cpgi-3*$^{(-/-)}$ mutant in the progeny after feeding *cpgi-3*$^{(+/-)}$ flowers with sugars via floral dipping.

Supplemental Table S5. Total seeds were harvested from the sugar-fed siliques and visually classified into three groups based on seed morphology and size (please see Supplemental Figure S8 for the image).

Supplemental Table S6. The *cpgi*$^{(-/-)}$ mutants were isolated from the group of sugar-fed, small seeds germinated and grown on half-strength Murashige and Skoog, 0.5% Suc plates.

Supplemental Table S7. Primers used in this study.

Acknowledgments

We thank the Imaging Core Facility at the Institute of Molecular Biology, Academia Sinica, and Academia Sinica Advanced Optics Microscope Core Facility (AS-AOMCF) for technical support in microscopic imaging. The AS-AOMCF is funded by the Academia Sinica Core Facility and Innovative Instrument Project (AS-CFII-108-116). We also thank the Plant Cell Biology Core Lab at the Institute of Plant and Microbial Biology, Academia Sinica, for assistance in TEM. We are grateful to Ms. Chia-Chen Wu and Ms. Pei-Ying Chen for their technical assistance in Alexander staining and plant material preparation.

Funding

This work was supported by a grant from Academia Sinica, Taiwan (034007).

Conflict of interest statement. The authors declare no conflict of interest.

References

Alexander MP (1969) Differential staining of aborted and nonaborted pollen. Stain Technol **44**: 117?122

Armstrong SJ, Franklin FCH, Jones GH (2003) A meiotic time-course for Arabidopsis thaliana. Sexual Plant Reprod **16**: 141–149

Bahaji A, Almagro G, Ezquer I, Gámez-Arcas S, Sánchez-López ÁM, Muñoz FJ, Barrio RJ, Sampedro MC, De Diego N, Spíchal L, et al. (2018) Plastidial phosphoglucose isomerase is an important determinant of seed yield through its involvement in gibberellin-mediated reproductive development and storage reserve biosynthesis in Arabidopsis. Plant Cell **30**: 2082–2098

Barratt DHP, Derbyshire P, Findlay K, Pike M, Wellner N, Lunn J, Feil R, Simpson C, Maule AJ, Smith AM (2009) Normal growth of Arabidopsis requires cytosolic invertase but not sucrose synthase. Proc Natl Acad Sci USA **106**: 13124–13129

Beeler S, Liu H-C, Stadler M, Schreier T, Eicke S, Lue W-L, Truernit E, Zeeman SC, Chen J, Kötting O (2014) Plastidial NAD-dependent malate dehydrogenase is critical for embryo development and heterotrophic metabolism in Arabidopsis. Plant Physiol **164**: 1175–1190

Chen L-Q, Lin IW, Qu X-Q, Sosso D, McFarlane HE, Londoño A, Samuels AL, Frommer WB (2015) A cascade of sequentially expressed sucrose transporters in the seed coat and endosperm provides nutrition for the Arabidopsis embryo. Plant Cell **27**: 607–619

Chen P-Y, Wu C-C, Lin C-C, Jane W-N, Suen D-F (2019) 3D imaging of tapetal mitochondria suggests the importance of mitochondrial fission in pollen growth. Plant Physiol **180**: 813–826

Chen R, Zhao X, Shao Z, Wei Z, Wang Y, Zhu L, Zhao J, Sun M, He R, He G (2007) Rice UDP-glucose pyrophosphorylase1 is essential for pollen callose deposition and its cosuppression results in a new type of thermosensitive genic male sterility. Plant Cell **19**: 847–861

Clough SJ, Bent AF (1998) Floral dip: a simplified method for Agrobacterium -mediated transformation of *Arabidopsis thaliana*. Plant J **16**: 735–743

Cogoni C, Macino G (1997) Conservation of transgene-induced post-transcriptional gene silencing in plants and fungi. Trends Plant Sci **2**: 438–443

Comparot-Moss S, Kotting O, Stettler M, Edner C, Graf A, Weise SE, Streb S, Lue W-L, MacLean D, Mahlow S, et al. (2010) A putative phosphatase, LSF1, is required for normal starch turnover in Arabidopsis leaves. Plant Physiol **152**: 685–697

Custers JBM, Snepvangers SCHJ, Jansen HJ, Zhang L, van Lookeren Campagne MM (1999) The 35S-CaMV promoter is silent during early embryogenesis but activated during nonembryogenic sporophytic development in microspore culture. Protoplasma **208**: 257–264

Dong X, Hong Z, Sivaramakrishnan M, Mahfouz M, Verma DPS (2005) Callose synthase (CalS5) is required for exine formation during microgametogenesis and for pollen viability in Arabidopsis. Plant J **42**: 315–328

Egli B, Kölling K, Köhler C, Zeeman SC, Streb S (2010) Loss of cytosolic phosphoglucomutase compromises gametophyte development in Arabidopsis. Plant Physiol **154**: 1659–1671

Engelke T, Hirsche J, Roitsch T (2010) Anther-specific carbohydrate supply and restoration of metabolically engineered male sterility. J Exp Bot **61**: 2693–2706

Enns LC, Kanaoka MM, Torii KU, Comai L, Okada K, Cleland RE (2005) Two callose synthases, GSL1 and GSL5, play an essential and redundant role in plant and pollen development and in fertility. Plant Mol Biol **58**: 333–349

Gao F, Zhang H, Zhang W, Wang N, Zhang S, Chu C, Liu C (2021) Engineering of the cytosolic form of phosphoglucose isomerase into chloroplasts improves plant photosynthesis and biomass. New Phytol **231**: 315–325

Höfgen R, Willmitzer L (1988) Storage of competent cells for *Agrobacterium* transformation. Nucleic Acids Res **16**: 9877

Hofmann F, Schon MA, Nodine MD (2019) The embryonic transcriptome of Arabidopsis thaliana. Plant Reprod **32**: 77–91

Honys D, Twell D (2004) Transcriptome analysis of haploid male gametophyte development in Arabidopsis. Genome Biol **5**: 1–13

Hua Q, Yang C, Baba T, Mori H, Shimizu K (2003) Responses of the central metabolism in *Escherichia coli* to phosphoglucose isomerase and glucose-6-phosphate dehydrogenase knockouts. J Bacteriol **185**: 7053–7067

Huang T-H, Suen D-F (2021) Iron insufficiency in floral buds impairs pollen development by disrupting tapetum function. Plant J **108**: 244–267

Jones TWA, Gottlieb LD, Pichersky E (1986) Reduced enzyme activity and starch level in an induced mutant of chloroplast phosphoglucose isomerase. Plant Physiol **81**: 367–371

Jones TWA, Pichersky E, Gottlieb LD (1986) Enzyme activity in EMS-induced null mutations of duplicated genes encoding phosphoglucose isomerases in Clarkia. Genetics **113**: 101–114

Kötting O, Santelia D, Edner C, Eicke S, Marthaler T, Gentry MS, Comparot-Moss S, Chen J, Smith AM, Steup M, et al. (2009) STARCH-EXCESS4 is a laforin-like phosphoglucan phosphatase required for starch degradation in *Arabidopsis thaliana*. Plant Cell **21**: 334–346

Kawabe A, Yamane K, Miyashita NT (2000) DNA polymorphism at the cytosolic phosphoglucose isomerase (*PgiC*) locus of the wild plant *Arabidopsis thaliana*. Genetics **156**: 1339–1347

Kerschen A, Napoli CA, Jorgensen RA, Müller AE (2004) Effectiveness of RNA interference in transgenic plants. FEBS Lett **566**: 223–228

Kleczkowski LA, Decker D, Wilczynska M (2011) UDP-sugar pyrophosphorylase: a new old mechanism for sugar activation. Plant Physiol **156**: 3–10

Kleinboelting N, Huep G, Kloetgen A, Viehoever P, Weisshaar B (2012) GABI-Kat SimpleSearch: new features of the *Arabidopsis thaliana* T-DNA mutant database. Nucleic Acids Res **40**: D1211–D1215

Klepikova AV, Kasianov AS, Gerasimov ES, Logacheva MD, Penin AA (2016) A high resolution map of the *Arabidopsis thaliana* developmental transcriptome based on RNA-seq profiling. Plant J **88**: 1058–1070

Kozieradzka-Kiszkurno M, Płachno BJ (2012) Are there symplastic connections between the endosperm and embryo in some angiosperms?—a lesson from the Crassulaceae family. Protoplasma **249**: 1081–1089

Kunz H-H, Zamani-Nour S, Häusler RE, Ludewig K, Schroeder JI, Malinova I, Fettke J, Flügge U-I, Gierth M (2014) Loss of cytosolic phosphoglucose isomerase affects carbohydrate metabolism in leaves and is essential for fertility of Arabidopsis. Plant Physiol **166**: 753–765

Kunz HH, Häusler RE, Fettke J, Herbst K, Niewiadomski P, Gierth M, Bell K, Steup M, Flügge UI, Schneider A (2010) The role of plastidial glucose-6-phosphate/phosphate translocators in vegetative tissues of *Arabidopsis thaliana* mutants impaired in starch biosynthesis. Plant Biol **12**: 115–128

Lee JH, Chang KZ, Patel V, Jeffery CJ (2001) Crystal Structure of Rabbit Phosphoglucose Isomerase Complexed with Its Substrate d-Fructose 6-Phosphate. Biochem **40**: 7799–7805

Lemoine R, La Camera S, Atanassova R, Dédaldéchamp F, Allario T, Pourtau N, Bonnemain J-L, Laloi M, Coutos-Thévenot P, Maurousset L, et al. (2013) Source-to-sink transport of sugar and regulation by environmental factors. Front Plant Sci **4**: 272

Li D-D, Xue J-S, Zhu J, Yang Z-N (2017) Gene regulatory network for tapetum development in *Arabidopsis thaliana*. Front Plant Sci **8**: 1559

Li Y, Li L, Wang Y, Wang Y-C, Wang N-N, Lu R, Wu Y-W, Li X-B (2020) Pollen-specific protein PSP231 activates callose synthesis to govern male gametogenesis and pollen germination. Plant Physiol **184**: 1024–1041

Liu M, Shi S, Zhang S, Xu P, Lai J, Liu Y, Yuan D, Wang Y, Du J, Yang C (2014) SUMO E3 ligase AtMMS21 is required for normal meiosis and gametophyte development in Arabidopsis. BMC Plant Biol **14**: 153

Lu P, Chai M, Yang J, Ning G, Wang G, Ma H (2014) The Arabidopsis *CALLOSE DEFECTIVE MICROSPORE1* gene is required for male fertility through regulating callose metabolism during microsporogenesis. Plant Physiol **164**: 1893–1904

Ma H (2005) Molecular genetic analyses of microsporogenesis and microgametogenesis in flowering plants. Annu Rev Plant Biol **56**: 393–434

Ma H (2006) A molecular portrait of Arabidopsis meiosis. The Arabidopsis Book: e0095

Malinova I, Kunz H-H, Alseekh S, Herbst K, Fernie AR, Gierth M, Fettke J (2014) Reduction of the cytosolic phosphoglucomutase in Arabidopsis reveals impact on plant growth, seed and root development, and carbohydrate partitioning. PLoS ONE **9**: e112468

Meinke DW (1985) Embryo-lethal mutants of *Arabidopsis thaliana*: analysis of mutants with a wide range of lethal phases. Theor Appl Genet **69**: 543–552

Meinke DW, Sussex IM (1979) Embryo-lethal mutants of *Arabidopsis thaliana*: a model system for genetic analysis of plant embryo development. Dev Biol **72**: 50–61

Mori T, Kuroiwa H, Higashiyama T, Kuroiwa T (2006) GENERATIVE CELL SPECIFIC 1 is essential for angiosperm fertilization. Nat Cell Biol **8**: 64–71

Napoli C, Lemieux C, Jorgensen R (1990) Introduction of a chimeric chalcone synthase gene into Petunia results in reversible co-suppression of homologous genes *in trans*. Plant Cell **2**: 279–289

Nishikawa S, Zinkl GM, Swanson RJ, Maruyama D, Preuss D (2005) Callose (β-1,3 glucan) is essential for Arabidopsispollen wall patterning, but not tube growth. BMC Plant Biol **5**, https://doi.org/10.1186/1471-2229-5-22

Nowitzki U, Flechner A, Kellermann J, Hasegawa M, Schnarrenberger C, Martin W (1998) Eubacterial origin of nuclear genes for chloroplast and cytosolic glucose-6-phosphate isomerase from spinach: sampling eubacterial gene diversity in eukaryotic chromosomes through symbiosis. Gene **214**: 205–213

Owen HA, Makaroff CA (1995) Ultrastructure of microsporogenesis and microgametogenesis in *Arabidopsis thaliana* (L.) Heynh. ecotype Wassilewskija (Brassicaceae). Protoplasma **185**: 7–21

Park J-I, Ishimizu T, Suwabe K, Sudo K, Masuko H, Hakozaki H, Nou I-S, Suzuki G, Watanabe M (2010) UDP-glucose pyrophosphorylase is rate limiting in vegetative and reproductive phases in *Arabidopsis thaliana*. Plant Cell Physiol **51**: 981–996

Preiser AL, Banerjee A, Weise SE, Renna L, Brandizzi F, Sharkey TD (2020) Phosphoglucoisomerase is an important regulatory enzyme in partitioning carbon out of the Calvin-Benson cycle. Front Plant Sci **11**: 580726

Rottmann T, Fritz C, Sauer N, Stadler R (2018) Glucose uptake via STP transporters inhibits in vitro pollen tube growth in a HEXOKINASE1-dependent manner in *Arabidopsis thaliana*. Plant Cell **30**: 2057–2081

Sager R, Lee J-Y (2014) Plasmodesmata in integrated cell signalling: insights from development and environmental signals and stresses. J Exp Bot **65**: 6337–6358

Scholl RL, May ST, Ware DH (2000) Seed and molecular resources for Arabidopsis. Plant Physiol **124**: 1477–1480

Schreyer R, Böck A (1980) Phosphoglucose isomerase from Escherischia coli K 10: purification, properties and formation under aerobic and anaerobic condition. Arch Microbiol **127**: 289–298

Slewinski TL (2011) Diverse functional roles of monosaccharide transporters and their homologs in vascular plants: a physiological perspective. Mol Plant **4**: 641–662

Stone BA (2009) Chemistry of β-glucans. *In* A Bacic, GB Fincher, BA Stone, eds, Chemistry, Biochemistry, and Biology of 1-3 Beta Glucans and Related Polysaccharides. Academic Press, San Diego, CA, pp 5–46

Sun Y-J, Chou C-C, Chen W-S, Wu R-T, Meng M, Hsiao C-D (1999) The crystal structure of a multifunctional protein: Phosphoglucose isomerase/autocrine motility factor/neuroleukin. Proc Natl Acad Sci USA **96**: 5412–5417

Sunilkumar G, Mohr L, Lopata-Finch E, Emani C, Rathore KS (2002) Developmental and tissue-specific expression of CaMV 35S promoter in cotton as revealed by GFP. Plant Mol Biol **50**: 463–479

Thomas BR, Ford VS, Pichersky E, Gottlieb LD (1993) Molecular characterization of duplicate cytosolic phosphoglucose isomerase genes in Clarkia and comparison to the single gene in Arabidopsis. Genetics **135**: 895–905

Thomas BR, Laudencia-Chingcuanco D, Gottlieb LD (1992) Molecular analysis of the plant gene encoding cytosolic phosphoglucose isomerase. Plant Mol Biol **19**: 745–757

Thomson JG, Cook M, Guttman M, Smith J, Thilmony R (2011) Novel *sul* I binary vectors enable an inexpensive foliar selection method in *Arabidopsis*. BMC Res Notes **4**: 44

Totir M, Echols N, Nanao M, Gee CL, Moskaleva A, Gradia S, Iavarone AT, Berger JM, May AP et al. (2012) Macro-to-Micro Structural Proteomics: Native Source Proteins for High-Throughput Crystallization. PLoS ONE **7**: e32498

van der Krol AR, Mur LA, Beld M, Mol JN, Stuitje AR (1990) Flavonoid genes in petunia: addition of a limited number of gene copies may lead to a suppression of gene expression. Plant Cell **2**: 291–299

Vaucheret H, Béclin C, Elmayan T, Feuerbach F, Godon C, Morel J-B, Mourrain P, Palauqui J-C, Vernhettes S (1998) Transgene-induced gene silencing in plants. Plant J **16**: 651–659

Waese J, Fan J, Pasha A, Yu H, Fucile G, Shi R, Cumming M, Kelley LA, Sternberg MJ, Krishnakumar V, et al. (2017) ePlant: visualizing and exploring multiple levels of data for hypothesis generation in plant biology. Plant Cell **29**: 1806–1821

Weeden NF, Gottlieb LD (1982) Dissociation, reassociation, and purification of plastid and cytosolic phosphoglucose isomerase isozymes. Plant Physiol **69**: 717–723

Wilkinson JE, Twell D, Lindsey K (1997) Activities of CaMV 35S and NOS promoters in pollen: implications for field release of transgenic plants. J Exp Bot **48**: 265–275

Winter D, Vinegar B, Nahal H, Ammar R, Wilson GV, Provart NJ (2007) An "Electronic Fluorescent Pictograph" browser for exploring and analyzing large-scale biological data sets. PLoS ONE **2**: e718

Xue J-S, Yao C, Xu Q-L, Sui C-X, Jia X-L, Hu W-J, Lv Y-L, Feng Y-F, Peng Y-J, Shen S-Y, et al. (2021) Development of the Middle Layer in the Anther of Arabidopsis. Front Plant Sci **12**: 634114

Yim K-O, Bradford KJ (1998) Callose deposition is responsible for apoplastic semipermeability of the endosperm envelope of muskmelon seeds. Plant Physiol **118**: 83–90

Yu T-S, Kofler H, Häusler RE, Hille D, Flügge U-I, Zeeman SC, Smith AM, Kossmann J, Lloyd J, Ritte G, et al. (2001) The Arabidopsis *sex1* mutant is defective in the R1 protein, a general regulator of starch degradation in plants, and not in the chloroplast hexose transporter. Plant Cell **13**: 1907–1918

Yu T-S, Lue W-L, Wang S-M, Chen J (2000) Mutation of Arabidopsis plastid phosphoglucose isomerase affects leaf starch synthesis and floral initiation. Plant Physiol **123**: 319–326

Zhang W, Sun Y, Timofejeva L, Chen C, Grossniklaus U, Ma H (2006) Regulation of Arabidopsis tapetum development and function by *DYSFUNCTIONAL TAPETUM1* (*DYT1*) encoding a putative bHLH transcription factor. Development **133**: 3085–3095

Zhu J, Chen H, Li H, Gao J-F, Jiang H, Wang C, Guan Y-F, Yang Z-N (2008) *Defective in Tapetal Development and Function 1* is essential for anther development and tapetal function for microspore maturation in Arabidopsis. Plant J **55**: 266–277